Nuclear magnetic resonance on oriented rare-earth nuclei in rare-earth hosts: Application to [160]Tb

W. D. Brewer, P. Roman, M. Böttcher, and B. Illerhaus

Fachbereich Physik, Freie Universität Berlin, Arnimallee 14, D-1000 Berlin 33, Federal Republic of Germany

H. Marshak

U.S. National Bureau of Standards, Gaithersburg, Maryland 20899

K. Freitag and P. Herzog

Institut für Strahlen- und Kernphysik, Universität Bonn 1, D-5300 Bonn 1, Federal Republic of Germany

We summarize the application of nuclear magnetic resonance of oriented nuclei to rare-earth impurities implanted in ferromagnetic crystals of heavy rare-earth hosts. The experimental aspects are treated in some detail; we present results obtained on [160]Tb*Tb*, and give a formal description of the experiments. A discussion of extension to other, similar systems with applications in nuclear, solid-state, and low-temperature physics is given.

INTRODUCTION

The technique of nuclear magnetic resonance of oriented nuclei (NMR-ON) has been in use for many years.[1-3] Combining the spectroscopic precision of magnetic resonance with the sensitivity and selectivity of nuclear orientation detected by the anisotropy of nuclear radiations, it permits the determination of nuclear properties of radioactive isotopes and the study of hyperfine interactions in very dilute systems. The application of ion-implantation techniques,[4] especially on line with an accelerator or reactor, has greatly increased the number of nuclides which can be studied and has extended the lower limit on their half-lives down to a few seconds. Several groups throughout the world have constructed or are constructing large-scale facilities to permit such measurements.

Nevertheless, in examining the most recent compilation of NMR-ON experiments,[5] one is somewhat surprised to see how limited has been the range of host-impurity combinations to which the technique has thus far been applied. Of the more than 240 entries, about 95% were carried out with one of the $3d$ elemental ferromagnets (Fe, Co, Ni) as host lattice, $\frac{3}{4}$ of these being in Fe host. Furthermore, although 98 different isotopes of 34 elements have been subjected to NMR-ON, more than 80% of the latter are nd metals or sp metals and semimetals. Thus far, only three isotopes from the $4f$ series (and none from the $5f$ series) have been studied by NMR-ON. This is particularly surprising in view of the interesting nuclear physics in the lanthanoid region, where a transition from nearly spherical nuclei near doubly-magnetic [146]Gd to highly deformed nuclei is occurring. A number of determinations of nuclear moments (mostly magnetic moments) in this region using low-temperature nuclear orientation (NO) have been reported in recent years.[6-8] It would be particularly useful to find host-impurity combinations where both magnetic dipole and electric quadrupole interactions (and thus nuclear quadrupole moments) could be determined with high precision, and which would be suitable for on-line implantation experiments.

Some steps in this direction have been taken recently. Van Rijswijk et al.[9] have demonstrated NMR-ON on [141]Ce implanted into $3d$ ferromagnets, and Herzog et al. have observed NMR of oriented ^{177}Lu in iron.[10] Ebeling et al. have detected the resonance of ^{111}In implanted into gadolinium, demonstrating the application to lanthanoid host metals for the first time.[11] Moreover, following the pioneering experiments on [199]Au*Fe* by Callaghan et al.,[12] Hagn et al., and Ohya et al. have succeeded in resolving the electric quadrupole splitting by NMR-ON of several heavy-element impurities in cubic $3d$ ferromagnetic hosts.[13-15] Furthermore, after completion of the present work, we have learned that the latter group has also performed a true double-resonance experiment[16] on the quadrupole-split NMR spectrum of [188]Ir*Fe*.

In any case, these experiments do not permit a very precise determination of nuclear quadrupole moments, since the field gradients observed are not large and are generally not known from other measurements; furthermore, the quadrupole splittings may depend to a considerable extent on sample preparation. At best, one could hope to obtain quadrupole-moment ratios of limited precision by implanting series of heavy transition elements in hosts such as Fe, Co, or Gd and performing quadrupole-resolved NMR. The experiment of Ebeling et al.[11] is important in that it demonstrates the feasibility of implanting impurities into lanthanoid host crystals and observing their NMR, but the particular case chosen did not yield a resolvable quadrupole splitting of the resonance line. Gadolinium is similar to cobalt[17] in many of its magnetic properties, since the Gd ions are in an S state and exhibit only spin magnetism, so that quadrupolar effects are due only to the hexagonal lattice symmetry of the ions and conduction electrons. The hyperfine fields and nuclear spin dynamics of impurities in Gd can be expected to be similar to those observed in the $3d$ ferromagnetic hosts.[18]

In the remaining heavy lanthanoid (HL) hosts, the situation is very different, due to the large orbital moments of the $4f$ electrons. There are very strong magnetic anisotropies, and the nuclear spin-lattice relaxation is relative-

ly fast (it may be due predominantly to the Weger mechanism,[19,20] i.e., excitation of virtual spin waves by transitions between the nuclear sublevels, followed by decay of the spin waves with energy transfer to the conduction-electron bath). With $4f$ or $5f$ impurities in HL hosts, moreover, the unfilled nf shells produce large magnetic fields and electric quadrupole gradients, reduced only slightly from the free-ion values.[21] These interactions completely dominante the hyperfine splittings and should be largely independent of the details of sample preparation owing to the localized nature of the $4f$ (and to a lesser extent of the $5f$) orbitals.

The most important applications of on-line NMR-ON in heavy-lanthanoid hosts are to nuclear physics, especially the systematic determination of nuclear moments in the lanthanoid and actinoid regions. It should be mentioned, however, that in the lanthanoid region, in particular, serious competition in the measurement of nuclear moments comes from on-line laser spectroscopy.[22]

The study of lanthanoid-lanthanoid and actinoid-lanthanoid impurity-host combinations also yields information about the host's influence on the impurity hyperfine interactions, the chemical state of the impurities, spin-lattice dynamics, and spin-wave structures, as has already been demonstrated by spin-echo experiments on HL metals.[23,20,24−26] Furthermore, some of the HL metals containing radioactive impurity isotopes are of interest as absolute nuclear orientation thermometers for the very low-temperature region below 500 mK, especially for use in high external magnetic fields;[27] for this purpose, an accurate determination of their hyperfine parameters by NMR is essential. Nuclear decay-scheme studies are also greatly facilitated by such determinations.[28,29]

In this paper, we describe in detail the first experiments involving NMR-ON of implanted lanthanoid impurities in a HL host, using the model system ^{160}TbTb, and discuss possible applications to other HL hosts. For this system, the nuclear quadrupole splitting is large (of order 100 MHz), so that the quadrupole subresonances are widely spaced and very precise determinations of the quadrupole frequencies are possible. In order to observe two or more of the subresonances at low temperatures, a double-resonance experiment must be performed, with simultaneous application of radio-frequency power at several frequencies. Preliminary results have been reported in letters[30,31] which will subsequently be referred to as I and II, respectively.

EXPERIMENTS

Description and procedures

In these experiments, a high sensitivity to the NMR signal from a relatively small number of implanted impurity atoms is obtained by using radioactive impurity isotopes and detecting the nuclear orientation produced at low temperatures by means of the emitted γ-ray angular distribution. Nuclear resonance perturbs this angular distribution, i.e., changes the γ-ray counting rate in a particular direction as a function of applied radiofrequency (rf) power. The γ rays are usually detected by using a high-resolution semiconductor detector, and NMR spec-

tra are obtained as plots of counting rate versus rf frequency with signal averaging as necessary.

The isotope ^{160}Tb decays with a 72-d half-life, emitting β particles and a number of γ rays; for the NMR detection, only two prominent γ rays at 299 and 1272 keV were employed. The pulses corresponding to these γ rays were electronically sorted out of the amplified pulse spectrum from the detector and were accumulated as a function of rf frequency by a computer-controlled data-acquisition system, which also programmed the rf generators and the frequency modulation (fm) of the rf input. Figure 1 gives a block diagram of the detection, data acquisition, and radio frequency systems used for the double-resonance experiments. Because of the considerable inhomogeneous broadening of the resonance lines in these ferromagnetic metal hosts, the rf input must be frequency modulated to observe an NMR signal. To eliminate to first order the effects of nonresonant sample heating by the rf power, alternate count-rate measurements are made with and without fm and the difference is used to display the NMR spectrum. Additional corrections for nonresonant background were applied in the present work, as described below.
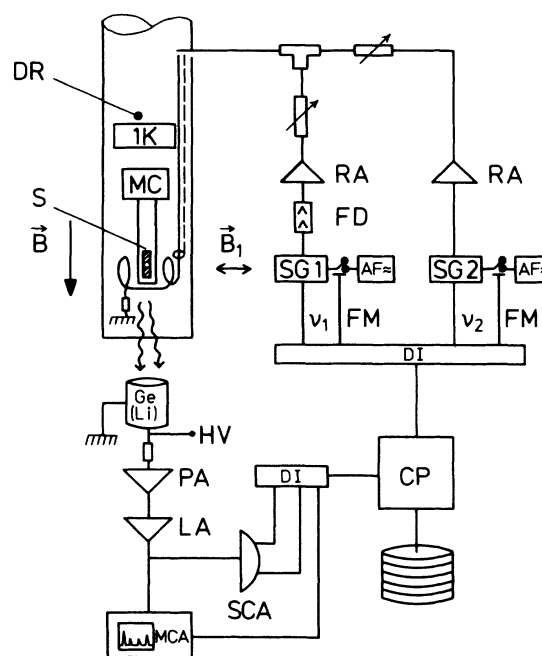

FIG. 1. Block diagram of the electronics used in the NMR-ON experiments. DR is a dilution refrigerator which cools the sample S in the applied field B. γ rays at $\theta=0$ (parallel to the sample b axis) are detected by the Ge(Li) detector and the corresponding pulses are amplified and selected by the amplifiers PA and LA and the single-channel analyzers (SCA). The energy spectrum can be recorded by a multichannel analyzer (MCA). The counting rates for particular γ rays, as well as the entire pulse-height spectrum, can be stored by the microcomputer (CP) via a digital interface (DI). This computer also controls the two rf signal generators SG1 (Schomandl MS 200M) and SG2 (Rohde & Schwarz SMPC) and the frequency modulation (audio generators AF). The rf signals are frequency-doubled (FD) as necessary, amplified by broadband amplifiers RA, and combined in an rf tee before entering the coaxial line to the 50-Ω coils around the sample.

The nuclear orientation of ^{160}Tb in Tb host has been investigated by several groups.[28,32,33] Our own results, along with a description of the cryogenic techniques required to achieve a significant degree of nuclear orientation in this system, are reported in detail elsewhere.[27,33] In the present experiments, the samples could be cooled continuously to about 10–12 mK by a dilution refrigerator, but were warmed to 20–25 mK by the applied rf power. At these temperatures, the γ rays used for NMR detection exhibit about a 30% change in counting rate in the direction of the sample magnetization, relative to the isotropic (high-temperature) rate.

Sample preparation

The samples used in this work were prepared starting from a large high-purity Tb single-crystal button obtained from Ames Laboratories (Ames, IA, USA).[34] A disk-shaped slab approximately 35 mm in diameter and 1.5-mm thick with c axis perpendicular to its face was spark cut from the button. From one-half of this disk, six rectangular samples measuring 4.5×10 mm were spark cut with the b axis (easy axis of magnetization) along the long dimension. These six samples were designated by the letters $A-F$. Both of the flat faces of each sample were spark planed and then polished with diamond powder, the final polishing being done with a particle size of 0.2–1 μm. The thickness of the finished samples was 1 mm. Two of the samples (A and C) were electropolished using a perchloric acid-methanol electrolyte at $-70\,°$C for 5 s at 35 V. Extensive x-ray diffraction analysis was done on sample D to ensure that it was a good single crystal with the correct crystallographic alignment. Less extensive x-ray analysis was done on three of the remaining samples. All of the Laue patterns were essentially

identical except that from the electropolished sample; the sharpness of the diffraction pattern indicates very little mosaic spread, and uncertainty in the crystallographic alignment was estimated to be about $\pm 1°$. The electropolished sample showed both in microscopic examination and in x-ray diffraction evidence of pitting and loss of crystallographic alignment; such samples are known to be covered by a chloride layer which prevents oxidation and maintains a bright metallic appearance to the eye.

The back face of each sample was tinned with pure indium and soldered to a high-purity copper sample holder which was later provided with a nuclear orientation thermometer (^{54}MnAu); these holders were mounted on the cold finger of the dilution refrigerator using In-Ga eutectic solder.

The radioactive ^{160}Tb impurities were introduced into the samples in two ways. Samples D and F were "bulk" samples, used for comparative nuclear orientation experiments. They were activated in situ by irradiation with a thermal neutron flux of 1.3×10^{13} (s cm^2)$^{-1}$ at the NBS reactor. During the irradiation, the ends of sample F were protected by Cd "boots" so that only the central portion was irradiated, giving a region of homogeneous, constant demagnetization factor. The final activities were about 8×10^5 Bq, corresponding to a concentration of <0.01 ppm in the active regions. Radiation damage due to thermal neutrons is minimal and spread throughout the bulk of the crystal, so that these samples could be considered to represent "perfect" lattices with extremely dilute impurities. High-precision nuclear orientation data for 22 γ rays from sample F in the temperature range 18–150 mK, using resistance thermometry with superconducting fixed-point calibration, are described in Ref. 33 and will be quoted below for

TABLE I. Sample preparation and properties.

Sample	Surface treatment	Activation	Heat treatment	Site fraction f
$A\,1$	electropolish	implant, 80 kV ca. 5×10^{12} cm^{-2}	none	0.2 (B dependence)
$B\,1$	diamond polish, 1 μm	implant, 80 kV ca. 5×10^{12} cm^{-2}	none	0.49(5)
D	diamond polish, 1 μm	neutron irradiated	none	ca. 1 (demagnetization) correction)
$A\,1$	diamond polish, 0.2 μm	implant, 80 kV ca. 10^{13} cm^{-2}	none	0.24(3)
$B\,2$	diamond polish, 0.2 μm	implant, 80 kV ca. 10^{13} cm^{-2}	none	0.23(3)
F	diamond polish, 1 μm	neutron irradiated (masked)	none	1.00
$A\,3$	diamond polish, 0.5 μm	implant, 160 kV (weak)	none	
$B\,3$	diamond polish, 0.5 μm	implant, 160 kV ca. 5×10^{13} cm^{-2}	none	0.63(6)
$E\,3$	diamond polish, 0.5 μm	implant, 160 kV ca. 5×10^{13} cm^{-2}	none	0.65(6)
$B\,3'$	diamond polish, 0.5 μm	implant, 160 kV ca. 5×10^{13} cm^{-2}	2 h, 600 °C pure Ar	0.35(5)
$E\,3'$	diamond polish, 0.5 μm	implant, 160 kV ca. 5×10^{13} cm^{-2}	2 h, 600 °C vacuum	0.40(5)

comparison to the results from the NMR samples. The other half of the original large disk was used for studies of the low-temperature magnetization behavior, which will be reported elsewhere (see Ref. 35).

The remaining samples A, B, and E were activated by implantation of ^{160}Tb ions using the Bonn isotope separator.[36] Three series of implantations were performed, which we denote as 1–3, giving samples $A1$, $B2$, etc. 2.5 mg of Tb_2O_3 were irradiated with thermal neutrons to give about 2×10^8 Bq of ^{160}Tb activity. This material was introduced into a tubular graphite oven in a Nielson-type ion source of the isotope separator; there, by the method of internal chlorination[37] with CCl_4, it was chemically converted, vaporized, dissociated, and ionized at temperatures around 800 °C. After mass separation from the stable ^{159}Tb ions with an enrichment factor of order 10^3, ^{160}Tb ions were implanted into a central spot (defined by a circular mask of about 3 mm diam) on the polished faces of the Tb crystal slabs. Total implanted doses were between 5×10^{12} and 5×10^{13} ions cm^{-2}, giving radioactivities of about 6×10^5 Bq. In the implantation series 1 and 2, an accelerating voltage of 80 kV was applied to the Tb ion beam; in series 3, by applying a postacceleration with another 80 kV, the total accelerating voltage was increased to 160 kV. The resulting implantation energies for singly charged ions are 80 and 160 keV, and the corresponding average implantation depths are about 17 and 35 nm, respectively. The results for all the samples prepared are summaried in Table I.

The expected γ-ray anisotropy can be calculated from the hyperfine interactions, the sample temperature, and the nuclear decay properties (see next section); this calculated anisotropy was in fact observed in the "bulk" sample F. All the implanted samples showed a reduction of the anisotropy compared to that expected, and we have characterized the reduction in Table I by the factor f. In a simple two-site model, f is the fraction of the impurities occupying undisturbed lattice sites, which contribute the full γ-ray anisotropy. The remaining fraction $1-f$ is assumed to be in disturbed sites which give rise to zero anisotropy when averaged over the sample. This model is, of course, not unique; however, since in most cases f was found to be constant for a given sample over a wide range of temperatures and applied magnetic fields (typically 10–40 mK, 0.5–3 T), it is at least a reasonable description of the anisotropy reduction. We can offer three possible explanations for the observed reductions.

(1) The fraction $1-f$ of the impurity ions is implanted into the oxide layer which inevitably covers the crystal surface. There, they are subject to poor thermalization and it is difficult to produce a macroscopic quantization axis (i.e., saturated magnetization). These impurities thus contribute on the average zero γ-ray anisotropy.

(2) Some fraction of the ions is implanted into a metallic but disturbed (polycrystalline, amorphous, or pitted) layer left by the surface treatment of the sample. In this case, thermalization should be good but the layer is likely to be magnetically hard, so that the apparent f will increase with increasing applied field.

(3) Impurity-associated defects produced by the implantation itself disturb the local lattice structure near the impurities and give rise to sites with reduced or vanishing anisotropy.

We can distinguish among these possibilities by examining the effects of surface treatment of the crystals before implantation, of implantation energy, and of thermal treatment after the implantation. Since the "impurities" in the present case are electronically and chemically identical to the host-lattice ions, defects should show no preference for association with the impurities and the effect of annealing should be to reduce the overall defect concentration and therefore increase f, if hypothesis (3) is significant. Samples $B3'$ and $E3'$ (Table I) were identical to $B3$ and $E3$, except that they were annealed for 2 h at 600 °C after the initial measurements. (Sample $B3'$ was annealed in high-purity Ar atmosphere, and $E3'$ in an oil-free vacuum of < 1.5 μPa.) In both cases, f was *reduced* by annealing; we attribute this to an increase in the oxide layer thickness during the annealing process. We conclude that at these dose rates, damage resulting from the implantation is not significant (and this is very probably true of other lanthanoid–heavy-lanthanoid combinations as well). This is also supported by the insensitivity of the NMR results to annealing as described below.

Hypothesis (2) should result in an applied-field dependence of f, which was observed only with sample $A1$, the electropolished sample. It therefore seems likely that the observed reductions for the other samples were due to implantation into the oxide layer; this is supported by the increase of f on increasing the average implantation depth. The small values of f seen in samples $A2$ and $B2$ are probably due to incomplete removal of the oxide layer from crystals A and B before repeating the implantation, possibly associated with the use of methanol for rinsing them.

This anisotropy reduction is not of critical importance for the NMR measurements; it produces only a corresponding decrease in signal-to-noise ratio in the frequency spectra, which, however, is tolerable. The impurity nuclei in disturbed sites are shifted far outside the resonant regions and contribute only a flat background to the spectra. However, these considerations *are* important for possible future applications to on-line NMR-ON. It would be advantageous to use a high accelerating voltage (we note that in Ref. 11, the In impurity ions were implanted into Gd crystals at 350 keV), to provide a means of cleaning the sample surface *in situ* immediately before beginning the implantation, and to maintain a clean vacuum in the sample chamber as far as possible. Electropolishing and contact with methanol should be avoided.

RESULTS

Formal description

The literature contains a number of confusing, inconsistent, and sometimes incorrect formulas for NMR with mixed magnetic-dipole–electric-quadrupole interactions. Therefore, we shall develop the formalism in some detail in this section to establish a firm basis for the following discussion.

Treatments of NMR in the presence of mixed magnetic dipole and electric quadrupole interactions have been given by Abragam,[38] Bleaney,[23] and Barnes,[39] among others; the latter two articles apply particularly to lanthanoid metals. Discussions of experiments relating to nuclear orientation and NMR-ON in the case of mixed interactions were published by Stone et al.[40,41] and more recently by Hagn.[42,43] NMR experiments on HL metals and alloys were performed by Sano and Itoh,[20,24,25] by Mackenzie et al.,[26] by Seiwa et al.,[44] and by Durand and Robert.[45] An excellent review was given by McCausland and Mackenzie.[46]

The Hamiltonian for a magnetic dipole and a coaxial electric quadrupole hyperfine interaction (HFI) is given by

$$\mathcal{H} = -g\mu_N \mathbf{B}_{eff} \cdot \mathbf{I}_z + \left[\frac{3e^2qQ}{4I(2I-1)} \right] \left[I_z^2 - \frac{I}{3}(I+1) \right] . \quad (1)$$

We choose the quantization axis z to be parallel to the externally applied magnetic field $\mathbf{B}$, as is usual in NO experiments. In the HL (except Gd), this is equivalent to choosing z parallel to the hyperfine field $\mathbf{B}_{hf}$, since the dominant contribution to the latter is the positive orbital field of the $4f$ electrons.[23] (Note that in the NMR literature, it is customary to write the magnetic HFI term as $+aI_z$, where $a = A\langle J_z \rangle$, with $A > 0$ when B_{hf} and the nuclear g factor are positive. This is tantamount to choosing z along $\mathbf{B}_{hf}$, because the ionic spin $\mathbf{J}$ is antiparallel to $\mathbf{B}_{hf}$ and thus $\langle J_z \rangle$ is negative with this choice of quantization axis. Choosing $a > 0$ when $gB_{hf} > 0$ is equivalent to taking z parallel to $\mathbf{J}$.) The various contributions to B_{hf} are discussed in Refs. 23 and 46; except in the S-state ions Gd^{3+} and Eu^{2+}, the total field is large (of order > 100 T) and positive. B_{eff} also contains the internal field given by $(1+K)(\mathbf{B} - \mathbf{B}_M)$, depending on the applied field $\mathbf{B}$. Here, K is the Knight shift of order 1% and thus unimportant for the experiments described below, and $\mathbf{B}_M$ is the demagnetizing field of the sample. This formula applies to a magnetized sample with $B > B_M$; the internal field then increases linearly with B. As B is lowered, the internal field is reduced in a way which depends on the magnetic history of the sample.

The quadrupole term contains the product of the electric field gradient (EFG), denoted as q (i.e., its negative component along the symmetry axis z') and the nuclear quadrupole moment Q (the projection of the quadrupole distortion of the nuclear charge distribution onto z'). The EFG is dominated by the ionic contribution $q_\parallel$ due to the $4f$ electrons,[23] which is parallel to the electronic magnetization, so that z' and z are collinear in a fully magnetized sample. A much smaller contribution $q_\perp$ is produced by the lattice ions and conduction electrons; its symmetry axis is the hexagonal c axis. In axially-anisotropic ferromagnets such as Tb, Dy, and Ho, the magnetization remains essentially in the basal plane, and is thus always perpendicular to c. The lattice term $q_\perp$ can then be treated as a perturbation, with

$$q = q_\parallel + q_\perp P_2(\cos\theta) ,$$

where $\theta = 90°$, i.e.,

$$q = q_\parallel - q_\perp/2 .$$

The magnetic HFI splits the nuclear state into $2I+1$ equally spaced sublevels labeled by the magnetic quantum number M_I, so that a single NMR line at the Larmor frequency ν_L results. The quadrupole term adds an additional shift depending on the value of $|M_I|$, which splits the NMR line into $2I$ subresonances symmetrically spaced around ν_L; their spacing depends on the quadrupole energy $h\nu_Q = e^2qQ$. Since the quadrupole shift is independent of the sign of M_I, its actual effect on the resonances must be independent of the sign of the magnetic HFI or the choice of the sign of the quantization axis. This is illustrated by the schematic energy-level diagrams in Fig. 2.

Formulas for the subresonance frequencies have been given by numerous authors,[38,39,43,46] generally in terms of the quantum number M_I. These expressions depend on the sign of g and on the choice of sign of the quantization axis and lead to confusing results if this is not correctly taken into account; e.g., they may yield negative resonance frequencies. Hagn[42,43] recognized the need to specify which of the M_I states is lowest in energy, but his formula can also give the wrong sign of the subresonance frequency. This is usually irrelevant in conventional NMR experiments, where typically the sign of ν_Q is not determined and the temperature is sufficiently high $(T > 1$ K) that all of the M_I sublevels are essentially equally populated. It is, however, very important in NO and NMR-ON experiments, where extreme population differences are produced and used to determine the sign of the quadrupole interaction. We thus prefer to give the subresonance frequencies in terms of the index n which labels the
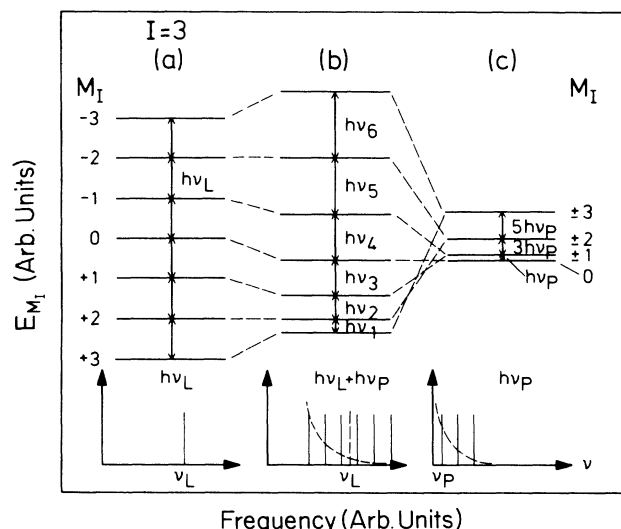

FIG. 2. Sublevel splittings for a nucleus of spin $I = 3$ in the case of (a) a pure magnetic-dipole HFI; (b) a mixed electric-quadrupole–magnetic-dipole HFI; and (c) a pure electric-quadrupole HFI, shown for $g > 0$, $B_{hf} > 0$, and $\nu_P > 0$. The corresponding NMR spectra are indicated schematically in the lower part of the figure, the dotted lines showing the approximate thermal equilibrium populations of the relevant initial-state sublevels at low temperature. (Population inversions may be produced by nuclear magnetic resonance; see Ref. 43.)

$2I$ transitions $(n = 1, 2, \ldots, 2I)$. We require that v_n always be positive and that v_1 correspond to the transition between the energetically *lowest* pair of sublevels. To this end, we define the following quantities:

$$v_M = \frac{|g\mu_N B_{\text{hf}}|}{h}, \quad v_P = \frac{3e^2qQ}{4I(2I-1)h},$$

$$v_B = \frac{|g\mu_N|}{h}(1+K)(B - B_M),$$

$$c = I(I+1), \quad b = \text{sgn}(B_{\text{hf}}), \quad s = \text{sgn}(g).$$

Note that the magnetic interaction frequency v_M is always positive as defined; the dependence on the signs of g and B_{hf} is separated out into the parameters s and b. The term v_B gives the shift in the resonance frequency due to the applied field B. The Larmor frequency is given by $v_L = |bv_M + v_B|$. The quadrupole interaction frequency v_P can be either positive or negative, depending on the relative signs of q and Q, and is related to v_Q by

$$v_P = \frac{3v_Q}{4I(2I-1)}.$$

Using these definitions, we can write the energy eigenvalues of the M_I substates:

$$E_{M_I} = -sh(bv_M + v_B)M_I + hv_P\left[M_I^2 - \frac{c}{2}\right]. \quad (2)$$

The formula for the subresonance frequencies v_n meeting the above conditions is then

$$v_n = \frac{(E_{sb(I-n)} - E_{sb(I+1-n)})}{h}. \quad (3)$$

Inserting the energy eigenvalues from Eq. (2) and simplifying, we obtain

$$v_n = v_M + bv_B + v_P[2n - (2I+1)]. \quad (4)$$

This is similar to the formula given in I; as expected, the sign of the magnetic interaction has dropped out (except in the frequency shift term v_B, whose sign depends on whether B_{hf} is negative or positive, i.e., on b). Equation (4) is thus generally applicable, regardless of the signs of the magnetic HFI or the quantization axis. Examples of its application are seen in the work of Hagn *et al.* and Ohya *et al.* on heavy-element impurities in Fe and Ni, cited above. The asymmetry of the NMR-ON spectral[13-16] clearly indicates which sublevels are lowest in energy, and the location of the subresonance v_1 relative to v_L can be used with Eq. (4) to determine the sign of v_P.

The γ-ray anisotropy $W(T,\theta)$ at a given temperature T and observation angle θ relative to the quantization axis is given by the usual formula:[47]

$$W(T,\theta) = \frac{N(T,\theta)}{N_H} = 1 + A_2B_2(T)P_2(\cos\theta) + \cdots, \quad (5)$$

where $N(T,\theta)$ is the counting rate for a particular γ ray at T and θ, and N_H is the corresponding counting rate at a high temperature $(T \gg 1$ K$)$ at which the γ-ray distribution is isotropic. The coefficient A_2 depends on the nuclear decay scheme and experimental geometry, and is accurately known for the γ rays used in this work.[28,33]

$P_2(\cos\theta)$ is the Legendre polynomial of second degree, and $B_2(T)$ is a statistical tensor component which gives the amount of nuclear alignment (i.e., the second moment of the nuclear orientation distribution). The first moment of nuclear orientation, the nuclear magnetization or polarization, is proportional to $B_1(T)$; only even terms occur in Eq. (5), owing to parity conservation in nuclear γ decay. Higher-order terms [e.g., a $P_4(\cos\theta)$ term] are negligible in the present case (the 299- and 1272-keV γ rays used in this study are nearly pure $E1$), but often must be taken into account.

It is clear from Eq. (5) that a fraction f of impurity nuclei in sites giving the full nuclear orientation, with the remaining nuclei contributing only isotropic radiation, leads to an observed anisotropy W_{exp} given by $(1 - W_{\text{exp}}) = f[1 - W(T,\theta)]$. The anisotropy from a polycrystalline or amorphous sample, which is incompletely magnetized,[28,32] is found by averaging over $P_2(\cos\theta)$ and leads to a similar formula for W_{exp}, but with a generally field-dependent f. If a continuous distribution of hyperfine interactions is present in the sample, averaging over $B_2(T)$ will be required, leading to an additionally field- and *temperature*-dependent f. In the case of ^{160}Tb, with a ground-state nuclear spin of $I = 3$, the following explicit formulas hold for $B_1(T)$ and $B_2(T)$:

$$B_1(T) = \frac{1}{2}\sum_{M_I} M_I a_{M_I},$$

$$B_2(T) = \left[\frac{1}{2\sqrt{3}}\right]\left[\sum_{M_I} M_I^2 a_{M_I} - 2\right], \quad (6)$$

where a_{M_I} is the temperature-dependent normalized population of the M_Ith substate, given by

$$a_{M_I} = \frac{\exp\left[-\dfrac{E_{M_I}}{kT}\right]}{\sum_{M_I}\exp\left[-\dfrac{E_{M_I}}{kT}\right]}.$$
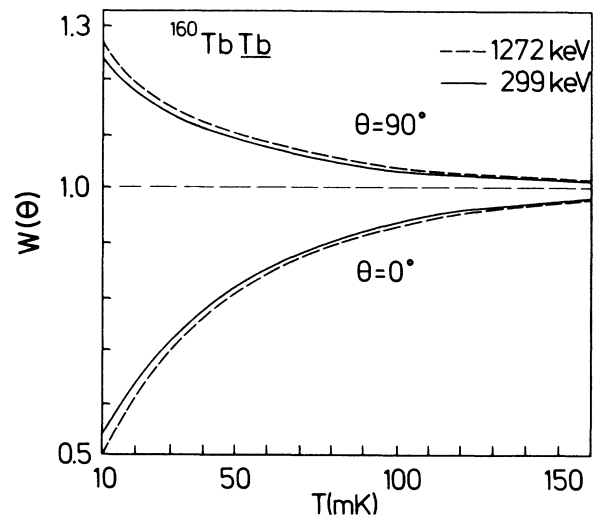

FIG. 3. γ-ray anisotropies (see text) at 0° and 90° for two γ rays from ^{160}Tb*Tb* as a function of sample temperature; from measurements on sample F (Ref. 33).

The anisotropies $W(T,0)$ and $W(T,90)$ of the 299- and 1272-keV γ rays from an ideal ^{160}TbTb samples (sample F) are shown in Fig. 3 for the temperature range 10–150 mK.

The NMR signal is conveniently defined[3] in terms of the change in γ-ray anisotropy observed on resonance, divided by the total available anisotropy at the given temperature:

$$S_n = \frac{[W(\text{fm},v_n)-W(v_n)]}{[1-W(v_n)]} . \tag{7}$$

It is also useful to define a relative signal R_n as the percentage change in counting rate on resonance compared to the nonresonant background:

$$R_n = \frac{100[N(\text{fm},v_n)-N(v_n)]}{N_H} . \tag{8}$$

In these formulas, the argument (v_n) implies that unmodulated rf at the frequency v_n is applied, giving rise to nonresonant heating to the operating temperature T, while (fm, v_n) means that the rf is frequency modulated, so that the NMR signal as well as nonresonant heating are present. The saturation NMR signals for different subresonances v_n can be readily calculated as a function of T using Eqs. (5), (6), and (8). The results are shown in Fig. 4 for a sample of substitutional fraction $f = 1.0$; it can be seen that while an appreciable signal R_1 at the resonance v_1 is to be expected over a wide temperature range, the signals for $n > 1$ (e.g., R_2) remain rather small. This is because the corresponding nuclear sublevels are hardly populated at low T where the nuclear orientation is considerable. At higher T, they are populated but lack of nuclear orientation reduces the observable signals. Detection of the higher resonances therefore requires a double-resonance experiment, where the v_1 resonance is
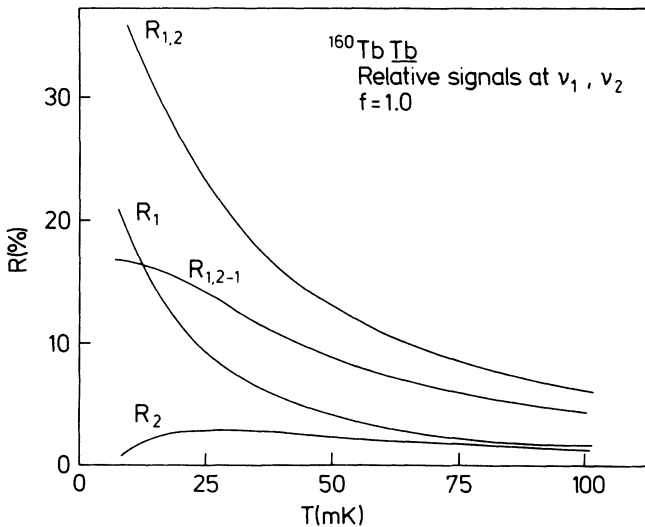

FIG. 4. Calculated relative NMR signals (defined in text) for a ^{160}TbTb sample of 100% site occupation ($f = 1$) as a function of temperature. R_1 and R_2 are for saturation of the corresponding subresonances alone; $R_{1,2}$ is the signal expected for simultaneous saturation of the first two subresonances; and $R_{1,2-1}$ is the incremental signal obtained from saturation of the second subresonance when the first has previously been saturated.

first saturated to populate the $M_I = |I-1|$ sublevel, and then rf at the frequency v_2 is applied to saturate the second resonance. The resulting signal for simultaneous saturation of the first two subresonances is indicated as $R_{1,2}$ in Fig. 4, and the incremental signal, due to saturation of v_2 after the v_1 resonance is already saturated, is given as $R_{1,2-1}$. The latter is seen to be even larger than the signal from v_1 alone in the temperature range of the present experiments. Simultaneous observation of the first three subresonances is in principle also possible, and would lead to an additional incremental countrate change of about 2% at 20 mK for ^{160}TbTb.

The actual NMR signal obtained depends not only on the sample temperature, but also on the strength and fm characteristics of the applied rf and on the nuclear spin-lattice relaxation time of the resonant nuclei. We define[48,49] an effective relaxation time τ_1 to be the time following an initial perturbation required for an observable (B_1 or B_2) to return to within $1/e$ of its equilibrium value $B_1(T)$ or $B_2(T)$. Such a definition is useful when the relaxation curves are not exponential, which is the case for relaxation of B_2 at all temperatures where this observable differs appreciably from zero, and, with a mixed magnetic-dipole-electric-quadrupole HFI, even for B_1 at the relatively high temperatures at which spin-echo experiments are usually performed.[20,25]

In order to maximize the NMR signal, the rf amplitude must be optimized, keeping nonresonant heating in mind. In the present case, the rf field amplitude B_1 [not to be confused with the nuclear polarization parameter $B_1(T)$] was about 2 μT, leading to sample heating from the base temperature of 10 mK to the operating range of 20–25 mK. The fm bandwidth Δ and frequency v_{fm} must also be optimized; Δ should be of the same order as the inhomogeneous NMR linewidth Γ_{inh} for an optimum signal, i.e., 3–4 MHz in the present case. In these experiments, we used triangle-wave modulation at the frequency v_{fm}, so that each frequency region in the range $v\pm\Delta/2$ is equally weighted. At low modulation frequencies, the effect of the fm can be considered in the time domain to be equivalent to a series of sweeps through the resonant region with a period $\tau = 1/v_{\text{fm}}$; if τ becomes long compared to τ_1, appreciable relaxation will occur between successive sweeps, and the time-averaged signal S_n will be reduced. In the limit $v_{\text{fm}}\rightarrow 0$, $\tau\rightarrow\infty$, S_n will vanish. This effect was studied some years ago for classical NMR-ON systems by Bacon et al.[48] and Wilson et al.[50] We can place their data for different systems on a "universal curve" if the normalized relative signal $\overline{R}$ is plotted against $v_{\text{fm}}\tau_1$, as has been done in Fig. 5. As can be seen, there is a rise in signal towards a saturation value as v_{fm} is increased; at high modulation frequencies, the signal again drops off. In the high-modulation-frequency limit, the effect of modulation is best considered[51] in the frequency domain: The carrier frequency at v is split into $2N+1$ sidebands over the region $v\pm\Delta/2$, spaced at intervals of v_{fm}. (N is the modulation index, $N=\Delta/2v_{\text{fm}}$.) The rf distribution thus forms a "comb" with gaps of order v_{fm} between the sidebands. When the homogeneous linewidth Γ of the local spin packets, governed by the
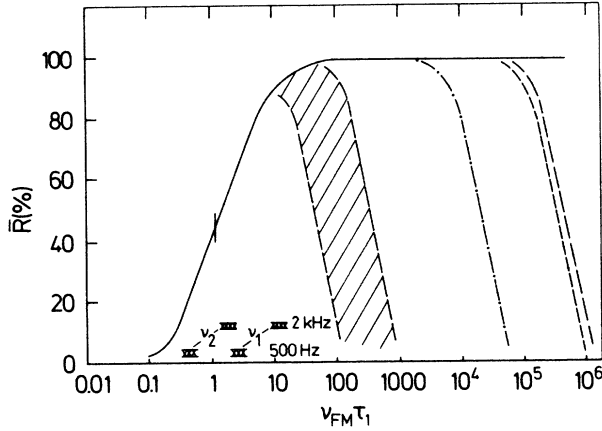
FIG. 5. The "universal curve" for the normalized cw NMR signal in a NMR-ON experiment as a function of the dimensionless parameter $\nu_{fm}\tau_1$. The dropoff at low-modulation frequencies is a result of nuclear relaxation as described in the text; that at high frequencies is due to the "gaps" in the Fourier spectrum of the modulated rf signal. The shaded region shows where the high-frequency dropoff might be expected for ^{160}Tb*Tb*. (See text; the large apparent variation in the dropoff curves for different systems is an artifact of this plotting method.) The vertical error bar indicates the uncertainty of the original data (Refs. 48 and 50). The cross-hatched regions show the parameter range for the first two subresonances in ^{160}Tb*Tb* at the two modulation frequencies given.

spin-spin relaxation time T_2 and by power broadening, is appreciably smaller than this gap width, some of the spin packets will fall into the gaps and signal will be lost if the oscillator is stable on a time scale of τ_1. This effect is seen in Fig. 5; the dashed curves indicate the dropoff in signal seen in two different experiments on ^{60}Co*Fe*, the chain curve was observed for ^{60}Co*Ni*, and the shaded region is the estimated corresponding dropoff region for ^{160}Tb*Tb*. The wide separation of the dropoff curves for different systems is in part an artifact of this plotting method, owing to the different relaxation times. (An unexpected feature of the curves is that the high-frequency dropoff occurs at higher values of ν_{fm} than expected from the probable linewidths Γ. In some cases, this may be due to additional interaction mechanisms which reduce T_2 and thus increase Γ; in most NMR-ON systems, where the extreme dilution of the sample nuclei precludes such spin-spin interactions, it is probably due to instabilities in the rf oscillator, which smear out the gaps in the rf comb. This was demonstrated in Ref. 48 by superimposing a second, lower-frequency modulation, thereby restoring the signal at high ν_{fm}.)

We can estimate the effective relaxation times for our samples by using the data of Ref. 20, where the relaxation of stable ^{159}Tb in Tb was studied. There, τ_1 for the $-\frac{3}{2} \rightarrow -\frac{1}{2}$ transition in ^{159}Tb was found to be about 0.07 ms at 1.35 K and zero applied field. The relaxation rates show a Korringa-like linear temperature dependence down to low temperatures, where they become temperature independent.[48,52] This is the case for τ_1 at a temperature given roughly[49] by $I\Delta E_{hf}/k$ (i.e., about 195 mK for ^{160}Tb*Tb*). Keeping this temperature dependence in mind,

and using the frequency and M_I dependence of the relaxation rate, we estimate τ_1 for the ν_1 transition in our system to be about 6.8 ms at low temperatures, while τ_1 for the ν_2 transition should be about 1.3 ms. (These estimates would remain valid for any magnetic relaxation mechanism.)

The applied-field dependence of the relaxation rates has not been determined in HL systems. However, most ferromagnetic alloys studied to date exhibit a relatively strong dependence of impurity-relaxation rates on applied magnetic field even at fields well above the value nominally required to saturate the samples.[49,53] It is generally agreed that the high-field limiting relaxation rates are the intrinsic ones, while additional relaxation channels occur at lower fields. One possibility is that the additional relaxation is due to fluctuations of the local magnetization; this is supported by the observed[49] dependence of the additional rate on the square of the ferromagnetic enhancement factor η:

$$\frac{1}{\tau_1} = r(B) = r_\infty + b\eta^2 , \qquad (9)$$

where

$$\eta = \left[1 + \frac{B_{hf}}{B_a + B} \right] . \qquad (10)$$

Here, η is the enhancement factor which describes the amplification of a fluctuating field at the impurity nucleus by the hyperfine field B_{hf}, and B_a is an "anisotropy field," a measure of the stiffness of the local magnetization [taken to be along an easy (b) axis in the basal plane, as was the case in our experiments] towards transverse fluctuations driven, for example, by the applied rf field B_1. These fluctuations are enhanced to give an oscillating field B_1(eff) at the nucleus. In the model for low-field relaxation, Eq. (9), the transverse components are due to random thermal fluctuations of the conduction-electron bath; the same enhancement thus enters the relaxation rate. In this equation, $r(B)$ and r_∞ are the relaxation rates in a moderate field B and at high field, and b is an experimentally-determined coefficient. The intrinsic rate r_∞ is usually reached for $B > 1$ T; an increase of a factor $a = r(0)/r_\infty$ (typically in the range $2 < a < 10$) occurs with decreasing field between 0.8 and 0.2 T.

The field dependence of the relaxation of each subresonance transition in a HL metal may be different, but we would expect the same basic characteristics to hold here, also. The estimated zero-field relaxation times τ_1 quoted above thus represent lower limits; note that they are considerably shorter than the usual low-temperature relaxation times found in $3d$ ferromagnetic hosts,[49] but comparable to what is seen in $4d$ enhanced ferromagnets.[53] This fast spin-lattice relaxation will provide rapid thermalization of implanted impurities for on-line applications.

Our initial experiments were carried out at $\nu_{fm} = 500$ Hz, and the corresponding values of $\nu_{fm}\tau_1$ are indicated in Fig. 5 as cross-hatched bars. As can be seen, the ν_1 resonance is within 70% of saturation; given the uncertainty in the field dependence of τ_1, it may well be in the plateau region. For ν_2, however, we are still in the region

of steep slope with only about 20% saturation. In fact, the second subresonance could not be observed at this modulation frequency, and was detected only after increasing ν_{fm} to several kHz. Even then, its behavior indicates that our signal may be relaxation limited and that still faster modulation should have been used, with an additional modulation superimposed to prevent signal dropoff due to gaps in the rf comb. This fact is of importance for future resonance experiments on the HL.

If the modulation conditions are adjusted to obtain a signal in the plateau (saturation) region of Fig. 5, the signals obtained are still limited by usable rf amplitudes. Wilson and Bosse[54] have calculated the resonance signals in this "fast-modulation" regime, finding a saturation parameter $\kappa = \gamma^2 B_1^2(\text{eff})\tau_1/\Delta$. The effective rf amplitude $B_1(\text{eff})$ is given by the applied amplitude B_1 and the rf enhancement factor η:

$$B_1(\text{eff}) = \eta B_1 = \left[1 + \frac{B_{hf}}{B_a + B}\right] B_1 \ . \tag{11}$$

We would therefore expect a resonance signal with rf field dependence given by Eq. (11) together with the field dependence of τ_1, Eq. (9); the two effects tend to compensate each other, since η decreases with increasing B, while τ_1 increases. The overall dependence, combining Eqs. (9) and (11), and neglecting the constant term in η [Eq. (10)] (an excellent approximation except at extremely high applied fields), is found to be

$$\kappa = c[aB_a^2 + 2B_aB + B^2]^{-1} \ , \tag{12}$$

where c is a constant equal to $\gamma^2 B_a^2 B_1^2[(a-1)/b]/\Delta$, and a and b are the coefficients of the field dependence of the relaxation rate defined above. These constants can be determined from a fit to the magnetic field dependence of the relaxation times, when it is known. The experimentally observed field dependence of the resonance signals was different for the first two subresonances, as will be seen in the next section.

Resonance data: ν_1 resonance

Based on the resonance frequencies[20] of stable ^{159}TbTb and on the reported ^{160}Tb- to ^{159}Tb-nuclear-moment ratios[55] we expected the first subresonance ν_1 from Eq. (4) to be in the frequency range 380–520 MHz. This region was searched using sample $B1$. Regions of about 40-MHz width were swept using $\Delta = 2$ MHz, $\nu_{fm} = 500$ Hz, and counting times of about 10 min per frequency point; the step width $\delta\nu$ between frequency points was 1.5 MHz, and each point was measured with and without fm as described above. A sweep thus required about 12 h, and several sweeps were added to improve statistics. With these rf conditions, a weak indication of a NMR signal was found near 480 MHz, but its identity was uncertain. Moreover, in spite of the use of difference spectra with and without fm, some residual heating effects were seen. These are due to power resonances in the rf system; if a relatively sharp peak in the rf power occurs as a function of frequency, the averaged power with fm will not be precisely the same as the power at the center frequency. In

particular, for a Gaussian power resonance, the measurements with fm will have a somewhat higher average power level than those without fm at the flanks of the power resonance line, and the converse will be true near the peak, giving rise to a double-dispersion-curve background shape in the difference spectra. One approach to avoiding this difficulty is to use a pickup coil or a resistance thermometer near the sample to measure the rf power directly and employ a feedback system to obtain power leveling. This introduces additional complications since the response of the power sampling circuit may also not be constant over a large frequency range, so that we chose instead to perform background corrections on the measured difference spectra to eliminate the small residual heating effects, as described below.

Samples A and B were repolished and reimplanted, giving samples $A2$ and $B2$. In spite of the relatively small values of f, these samples were used for further resonance searches, increasing the frequency steps to 2 MHz and the fm bandwidth Δ to 4 MHz, and improving the rf
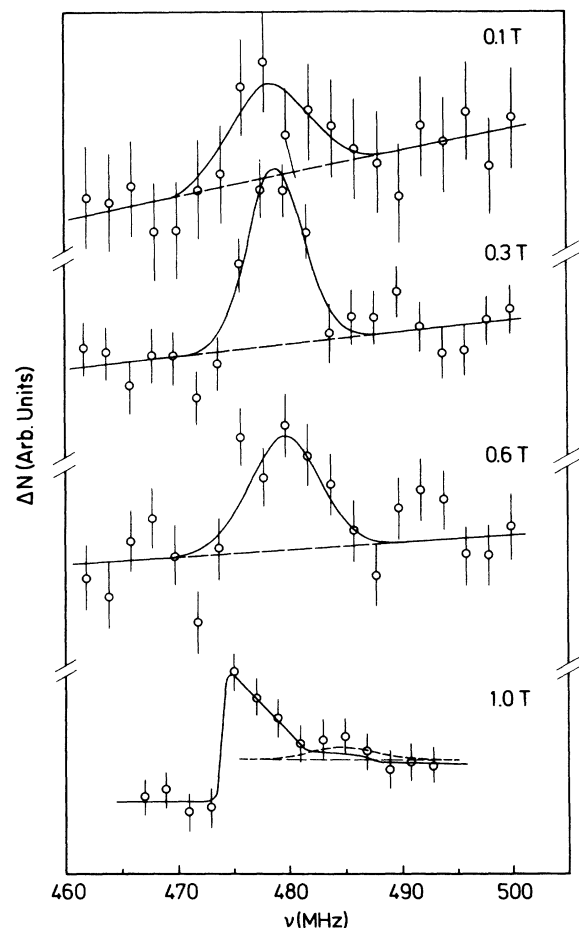

FIG. 6. Uncorrected data for the first subresonance in ^{160}TbTb; the counting-rate change with and without fm (in arb. u.; different spectra have different vertical scales) is plotted vs rf center frequency for the applied fields shown. The errors given are statistical; the lines are guides to the eye. The solid line in the 1.0-T spectrum is the background due to nonresonant heating (see text), while the dashed lines indicate the expected position and shape of the resonance; it is clearly not detectable at this applied field. Data are from sample $A2$.

W. D. BREWER *et al.*

input lines and coil to reduce power resonances. The signal at 480 MHz was verified, as shown in the raw difference spectra of Fig. 6 for several applied fields *B*. A strong applied field dependence of signal linewidth, position, and amplitude was observed, as expected from the above considerations. The structure seen at 1 T applied field and shifted to lower frequency than the resonance line has the typical shape expected from a narrow, asymmetric power resonance near 478 MHz; it was clearly visible in the data from the ^{54}Mn *Au* NO thermometer, and is therefore due to nonresonant heating. The NMR line at this applied field is probably too weak to be detected (dashed curve in Fig. 6). The background structure was thus subtracted from all the spectra, giving the results shown in Figs. 7 and 8. The properties of these corrected resonance curves, obtained from fits as shown in the figures, are summarized in Table II and Fig. 9. (In Tables II and III slight changes in the numerical values compared to those reported in II are due to reanalysis including more data as well as to the use of the frequencies
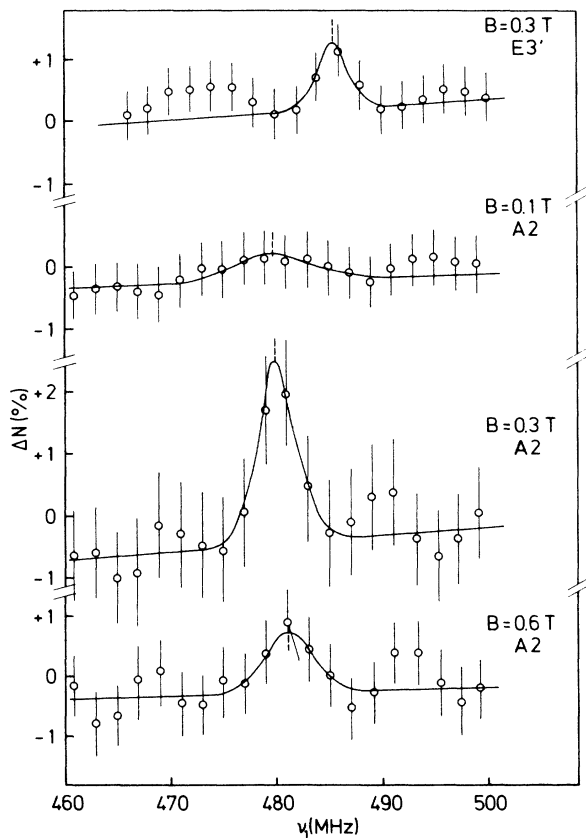

FIG. 8. A background-corrected NMR line for sample *A*2 at the first subresonance frequency taken at higher resolution (frequency step 1 MHz, fm bandwidth 3 MHz). The vertical scale is the same as in Fig. 7.

FIG. 7. The spectra of Fig. 6, corrected for the nonresonant background. At the top of the figure, the spectrum from sample *E*3' (annealed) is also shown; it was acquired at a higher modulation frequency and was not corrected for nonresonant heating (which probably produces the bulge at the left of the NMR line; it was shifted and flattened compared to that in Fig. 6 by modifying the rf coils). The applied fields and sample numbers are indicated; the vertical scale is the same for all spectra and gives the percent change in counting rate (299- and 1272-keV γ rays) relative to the isotropic rate. The solid lines are least-square fits to a Gaussian line plus linear background, and the dashed vertical lines show the fitted center frequencies (Table II).
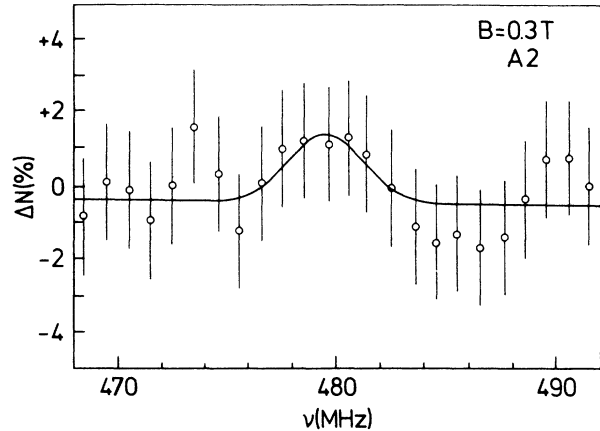
from the annealed samples.) The integrated, normalized relative signal strength $\bar{R}$ is found to decrease with increasing *B* and is described well by Eq. (11), i.e., assuming τ_1 to have only a weak field dependence, with $B_a = 0.42$ T. The latter value is close to that expected[32] for the basal-plane anisotropy of Tb from the measured magnetic anisotropy constants at 4.2 K.

The wide line and relatively weak signal seen at $B = 0.1$ T are not surprising; at this applied field, the samples are incompletely magnetized,[35] so that there is a spread of angles between the local quantization axes (parallel to B_{hf}) and the external field **B**. This will result in line broadening and a loss of NMR signal, effects which have been observed in numerous NMR-ON experiments.[3,11] The position of this resonance is also uncertain due to hysteresis effects, as indicated by the dashed line in the lower portion of Fig. 9. An external field applied to a virgin sample is initially shielded by the demagnetizing field, so that the resonance should follow the dashed line up to $B = B_M$ (which is estimated to be 0.34 T from our sample geometry; it should be constant over the central region containing the impurity nuclei). On reducing the applied field from the saturation value, as was done for the 0.1 T measurement, depending on magnetic hysteresis the resonance can lie anywhere between the dashed and the solid lines.

The effects discussed in Ref. 11 for Gd host in the *a*-*c* plane at low applied fields are inapplicable here. There, a shift in the hyperfine frequencies in magnetically unsaturated samples was expected because of the changing angle between the quadrupole field-gradient symmetry axis and the magnetic hf field (quantization) axis, and due to anisotropy of B_{hf} between the inequivalent *c* and *a* axes. (In Gd, the easy axis of magnetization is the hexagonal *c* axis, but a conical distribution of the local magnetization vectors is present in incompletely magnetized samples.) In the case of Tb in the basal plane, by contrast, the $4f$ quadrupole axis follows the magnetic axis, as discussed above, and the lattice quadrupole contribution always remains perpendicular to both; moreover, no ap-

preciable anisotropy in B_{hf} is expected betweeen the nearly equivalent a and b axes.

The solid line in the lower part of Fig. 9 has the slope corresponding to our value of the ^{160}Tb nuclear dipole moment, 4.548(18) MHz/T, and was adjusted to give the best fit to the points at 0.3 and 0.6 T (weighting by the errors shown). Its intercept with the dashed line (at B_M) gives the derived zero-field resonance frequency, 480.0(4) MHz.
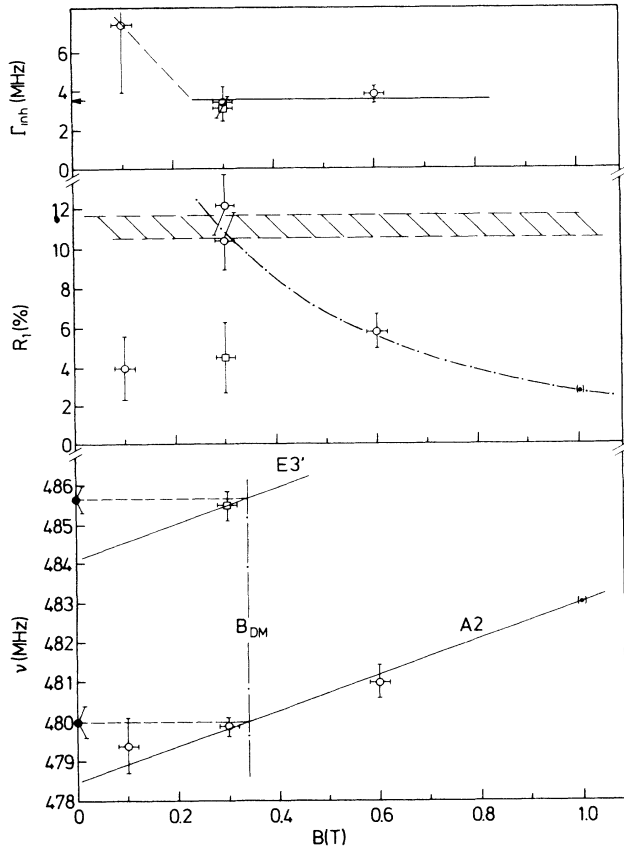

FIG. 9. Properties of the v_1 NMR lines (compare Table II); the circular points represent data from sample $A2$ (unannealed), the squares from sample $E3'$ (annealed). *Upper part*: The inhomogeneous linewidth (FWHM), corrected for fm broadening. The linewidth is not affected by annealing and is constant in magnetically saturated samples; the reasons for the broadening below 0.3 T are discussed in the text. *Middle part*: The relative signal, as in Fig. 4, normalized to the case of a sample with $f = 1$ to facilitate comparison of different samples. The shaded region represents the calculated saturation signal in the temperature range of the measurements. The dot-dashed line is the enhancement-factor dependence and is fitted to the points for sample $A2$ at 0.3 and 0.6 T. The reductions at 0.1 T and for the annealed sample are discussed in the text. *Lower part*: Field dependence of the resonance center frequencies. The solid lines have the predicted slopes for ^{160}Tb, 4.548 MHz/T (see below) and are adjusted to the data points; they give the expected dependence in a magnetically saturated sample. The dashed lines show the extrapolation to zero applied field (solid points with error bars). The shift between annealed and unannealed samples is discussed in the next section.

v_2 resonance

Because of the small site-occupation factors of samples $A2$ and $B2$, the double-resonance experiment was not attempted with these samples; instead, they were repolished and, together with a new crystal slab (E), were again implanted at an increased accelerating voltage of 160 kV. It was hoped that this higher voltage and consequent greater implantation depth would increase the site-occupation factor, as was indeed the case (Table I). Still higher voltages are clearly desirable. Sample $A3$ has a low-radioactive decay rate due to beam alignment difficulties during the implantation, so only $B3$ and $E3$ were used for further experiments. Again combining the spin-echo results on stable ^{159}TbTb with the nuclear-moment ratios reported by Easley et al. for ^{160}Tb$/^{159}$Tb, we obtain a predicted value for the magnetic frequency v_M in ^{160}TbTb equal to 1318(12.9) MHz. Together with our measured value of v_1, this led us to expect a quadrupole frequency v_P of 167.7(2.6) MHz and v_2 equal to 815(21) MHz. About the same time, the preliminary re-
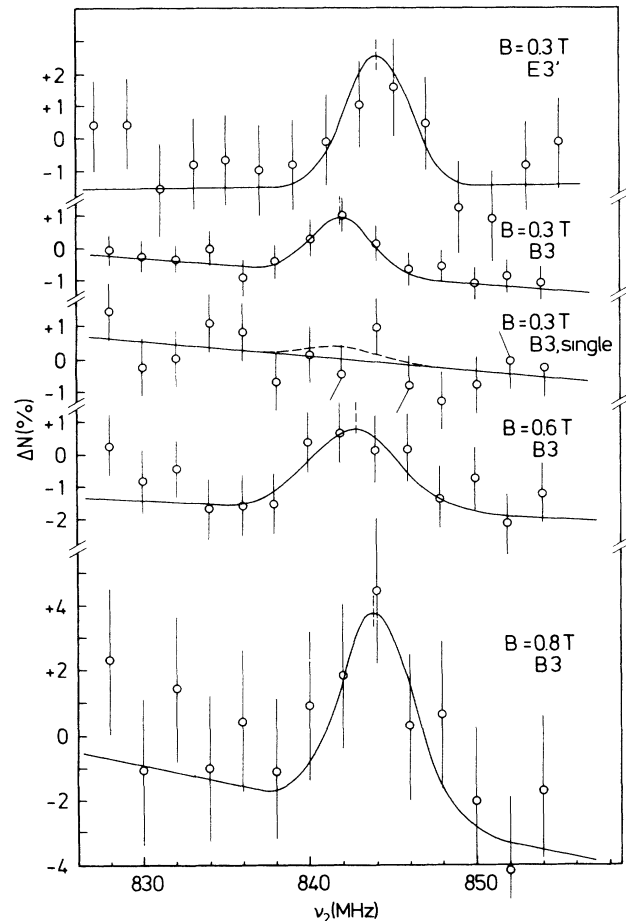

FIG. 10. NMR-ON resonance lines (notation similar to Figs. 7 and 8) for the second subresonance at v_2. These spectra were obtained at the applied fields and for the samples shown; the first subresonance was simultaneously saturated in all of the spectra except the one labeled "single." This curve shows the lack of a detectable signal at v_2 when the v_1 subresonance is not saturated; the expected signal (cf. R_2 in Fig. 4) is indicated as a dashed line. The resonance conditions were otherwise identical to those for the $B3$, 0.3 T curve.

TABLE II. Resonance line characteristics.

Sample	B (T)	ν_c (MHz)[a]	Γ_{inh} (MHz)[b]	R_{expt} (%)[c]	R (%)[d]
			ν_1 subresonance		
A2	0.1	479.4(7)	7.4(34)	0.95(42)	4.0(18)
A2	0.3	479.9(2)[e]	3.4(9)[e]	2.7(3)[e]	11.3(16)[e]
E3'	0.3	485.5(3)	3.2(7)	1.8(7)	4.5(18)
A2	0.6	481.0(4)	3.8(4)	1.4(2)	5.8(8)
			ν_2 subresonance		
B3	0.3	842.0(3)	3.4(5)	2.1(3)	3.3(5)
E3'	0.3	844.8(5)	3.6(5)	4.1(5)	10.3(12)
B3	0.6	843.7(5)	4.1(5)	2.5(4)	3.9(6)
B3	0.8	844.8(4)	5.0(17)	5.4(18)	8.4(28)

[a]Fitted center frequencies.
[b]Linewidths (FWHM) corrected for modulation broadening.
[c]Relative resonance signals (see text) as measured.
[d]Relative resonance signals normalized to a sample with $f = 1.0$.
[e]Averages of lines measured with fm bandwidths of 3 and 4 MHz (Figs. 7 and 8).

sults of precision NO measurements on sample F became available, and fits to their temperature dependence indicated somewhat higher hyperfine interaction frequencies, with ν_M above 1400 MHz and ν_P near 188 MHz.

Therefore, we searched for the second subresonance in the frequency region 780–880 MHz, using the arrangement shown in Fig. 1. A saturation signal at ν_1 was produced by rf generator 1 and a variable frequency in the 780–880-MHz range (with $\Delta = 4$ MHz, $\nu_{fm} = 500$ Hz, $\delta\nu = 2$ MHz) was applied by generator 2. Intensive searching failed to detect the second subresonance, as may be readily understood by referring to Fig. 5. When ν_{fm} was raised to about 2 kHz, a signal was detected near 840 MHz, as shown in Fig. 10. Here, no correction for nonresonant heating background was necessary, and the fits to the curves in Fig. 10 gave the resonance properties summarized in Table II and in Fig. 11. The final zero-field values for ν_1 and ν_2 from the unannealed samples are 480.0(40) and 842.40(26) MHz, respectively. From these, we can derive ν_M and ν_P independently, finding 1386.0(1.2) and 181.2(3) MHz (see Table III).

Finally, samples $B3$ and $E3$ were annealed as described above, giving samples designated as $B3'$ and $E3'$; the first two subresonances were detected in sample $E3'$, leading to the results shown in Figs. 7, 9, 10, and 11 and in Tables II and III. Both these resonances were observed with the same rf conditions as used for the ν_2 search. No significant linewidth changes were seen on annealing; the signal strength was considerably reduced at the ν_1 resonance (which may be a result of the higher modulation frequency, see below) but was increased for ν_2. A relatively large shift of the center frequency was seen at ν_1 (Fig. 9), while the shift at ν_2 was about half as large, indicating that the quadrupole frequency (which enters ν_1 with a larger coefficient) was mainly responsible for the observed shifts. Table III summarizes the zero-field resonance frequencies and the derived hyperfine interaction frequencies for all the experiments.

DISCUSSION

The resonance data obtained on the system ^{160}Tb*Tb* and described in the previous section demonstrate the

successful use of NMR-ON in the HL metals and illustrate the possibilities and limitations of the technique for studies in this region of the periodic table. We shall first discuss the characteristics of the resonance lines and try
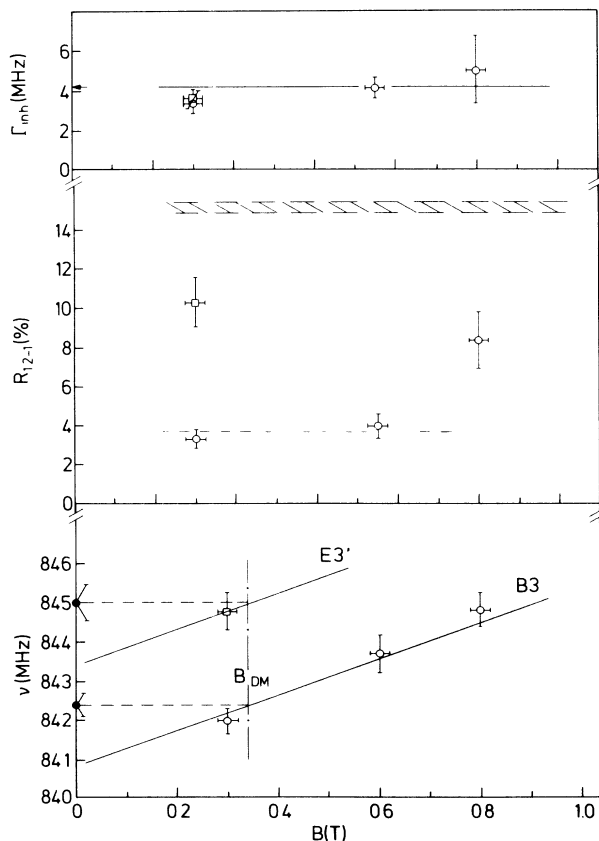

FIG. 11. Similar to Fig. 9 but for the NMR lines at ν_2 (Fig. 10 and Table II); the circles are for the unannealed sample $B3$, the square from annealed sample $E3'$. Again, the linewidth was constant as a function of applied field in saturated samples and did not change on annealing. The relative signal strength is here *larger* in the annealed sample than in the unannealed samples; also, it increases with increasing applied field. In the lower part, the field dependence of the NMR center frequencies and the extrapolation to zero field is shown. The shift between annealed and unannealed samples is smaller here than at ν_1.

TABLE III. Derived hyperfine frequencies and nuclear moment ratios.

Samples	v_1 (MHz)	v_2 (MHz)	v_M (MHz)	v_P (MHz)
B2, A3 (unannealed)	480.00(40)	842.40(26)	1386.0(12)	181.2(3)
E3′ (annealed)	485.65(32)	845.00(48)	1384.0(17)	179.7(4)
F[a] (bulk NO)			1393.8(81)	178.0(21)

Case	$r = g(^{159}\text{Tb})/g(^{160}\text{Tb})$	$R = Q(^{159}\text{Tb})/Q(^{160}\text{Tb})$
E3′/M[b]	2.254(5)	0.375(3)
E3′/S_1[b]	2.238(5)	0.370(3)
E3′/S_2[b]	2.312(7)	0.384(5)
NO/M[c]	2.239(24)	0.378(20)
ESR[d]	2.377(13)	0.48(8)

[a]Averages for 18 γ rays (Ref. 33).
[b]Using the HFI frequencies from the annealed sample compared to the results of Ref. 20: M, main line; S_1, and S_2, satellite lines from that work.
[c]Bulk NO (Ref. 33) compared to main line of Ref. 20.
[d]ESR of Tb doped into a Nd ethylsulfate crystal (Ref. 55).

to understand them in light of the formalism developed above. We then consider the comparison to other NMR data, and attempt to draw some conclusions concerning the general applicability of the method. Finally, we derive nuclear moments for ^{160}Tb and point out some particular aspects of the system studied.

Linewidths. The inhomogeneous linewidths observed in ferromagnetic samples with large electric quadrupole interactions are, in principle, due both to local variations in the magnetic HFI (transferred HFI from neighboring impurity atoms and lattice defects, variations in the demagnetizing field and the local magnetization with respect to the applied field) and to a spread of quadrupole interactions (local variations in lattice structure, e.g., due to defects). As pointed out above, the major part of the hyperfine interaction in lanthanoid–heavy-lanthanoid systems is produced by the open $4f$ shells, which, being well localized, are not expected to be sensitive to local environment effects. The spread in magnetic and electric HFI's is therefore caused by variations in the conduction-electron contributions to the hyperfine field and the field gradient, and in the lattice contribution to the latter, as well as by variations in the internal magnetic field. We observe an essentially constant linewidth in magnetically saturated samples, which is systematically but not significantly larger at the v_2 subresonance (arrows on the ordinate in Figs. 9 and 11). The fact that the linewidths of the two subresonances are not significantly different implies that a spread of quadrupolar frequencies is not a major contributor to the linewidth, since the quadrupole interaction enters v_1 with a coefficient of 5 but v_2 with a coefficient of only 3 [Eq. (4)]. In fact, the systematically wider lines at v_2 suggest a negative correlation between the magnetic and quadrupolar broadening effects: this is supported by the spin-echo results of Sano and Itoh[20] on ^{159}TbTb. Their central $(\frac{1}{2} \rightarrow -\frac{1}{2})$ line represents a purely magnetic splitting and shows a linewidth of about 15 MHz in both zero and 1.7 T applied fields, corresponding to 0.48% of the line-center fre-

quency of 3120 MHz. However, the lines resulting from the $(-\frac{1}{2} \rightarrow -\frac{3}{2})$ and $(\frac{1}{2} \rightarrow \frac{3}{2})$ transitions, which contain in addition the quadrupole frequency, are significantly narrower than the central line, again indicating an anticorrelation of magnetic and quadrupolar broadening effects. The corresponding magnetic linewidth in our case would be 6.7 MHz, about 60% larger than actually observed. This is not surprising, since we studied polished single-crystal samples, which should have a considerably smaller spread in internal fields than the powder samples of Sano and Itoh.

The constancy of the linewidths before and after annealing the samples is also consistent with this interpretation. Since a shift in the line centroids was observed, which we can attribute to a change in the average quadrupolar HFI, we might also expect a change in the quadrupolar broadening on annealing, as seen, for example, by Ebeling *et al.*[11] Any such change is, however, too small to be observable in the present experiments. Overall, the lines which we detected (width about 0.28% of the magnetic HFI frequency) are rather narrow in comparison to those usually found in $3d$ ferromagnetic hosts.[3] We attribute this to the careful sample preparation and use of single crystals in this work.

Center frequencies. The center frequencies of the resonance lines were found to shift as expected with applied magnetic field in saturated samples (Figs. 9 and 11). The relatively large shifts seen on annealing the samples can be associated with a small (not significant) shift in the magnetic HFI frequency (Table III), amounting to $\Delta v_M = -2.0(29)$ MHz or $-0.14(20)\%$, and a larger, significant shift in the electric quadrupole frequency, $\Delta v_P = -1.5(7)$ MHz or $-0.83(39)\%$. If the latter is attributed to the lattice- and conduction-electron part of the field gradient $q_\perp$, which was estimated by Bleaney[23] to correspond to about 3.5% of the total quadrupole splitting, we must assume an increase in $q_\perp$ of $+24(11)\%$ on annealing, presumably due to healing of lattice defects left by the implantation. The annealed samples should be

more representative of ideal, bulk material. This change of nearly 25% in the average lattice and conduction-electron field gradient is large but not out of the question, given the high concentration of defects present in the unannealed samples.

A direct comparison of our zero-field resonance frequencies to those of Sano and Itoh is problematic for a number of reasons, some of which have been discussed previously.[56] Their results were obtained on polycrystalline, powdered samples at temperatures above 1.35 K and mostly in zero applied field; the resonant nuclei were present at 100% concentration and resonance was detected by the rf signal from the precessing nuclear moments. Our measurements, in contrast, were done on high-purity, polished single crystals with a low concentration (50–400 ppm) of resonant nuclei, at $T < 25$ mK and in magnetically saturated samples, using an entirely different detection method (perturbation of the γ-ray anisotropy). The spin-echo spectra of Sano and Itoh were very broad, containing not only the wide, main resonance lines, but also satellite lines (S_1 and S_2) which were shifted by about -25 and $+80$ MHz, respectively, relative to the $(\frac{1}{2} \rightarrow -\frac{1}{2})$ main line. The lower satellite (S_1) was attributed to plate-shaped particles with a different demagnetizing field from the (predominantly) spheroidal ones, while the origin of S_2 remains unclear. A shift due to neighboring lanthanoid or oxide impurities was ruled out.[20] The entire distribution covers a frequency range of about 170 MHz at zero field and 80 MHz in 1.7 T applied field.

The second part of Table III contains the calculated ratios of magnetic dipole and electric quadrupole nuclear moments for ^{159}Tb/^{160}Tb obtained by comparison of the HFI frequencies from this work (annealed sample) with those of Sano and Itoh; the comparison was made for their main lines as well as for the two satellites. The table also shows the HFI frequencies deduced from fits to the temperature dependence of the NO from the bulk measurements, as well as the moment ratios reported by Easley *et al.*[55]; the latter magnetic-moment ratio differs by about 5% from that obtained in the present work combined with Sano and Itoh's main line. This discrepancy will be discussed in the concluding section.

Resonance signals. A major goal of this work was to demonstrate the feasibility of NMR-ON studies of lanthanoid–heavy-lanthanoid and actinoid–heavy-lanthanoid systems, especially in view of possible future applications in on-line implantation facilities. The resonance signal strengths obtainable under realistic cryogenic conditions with typical γ-ray counting rates and *rf* field amplitudes are thus of interest. In the spin-echo spectra,[20] the signal intensity remained nearly unchanged on going from zero applied field to 1.7 T; the authors attributed this to a cancellation of the effects of decreasing enhancement factor and increasing magnetization on increasing the applied field. Their polycrystalline powder samples were probably only about 70% magnetically saturated even at 1.7 T, while our samples were above 97% saturation at all fields used except 0.1 T. A similar argument thus does not apply to our results.

The behavior of the resonance signal on variation of

the applied field and on sample annealing is very different for the two subresonances, as pointed out in the previous section. At the ν_1 resonance ($+3 \rightarrow +2$ transition), the observed signals at 0.3 T essentially reached the calculated saturation value. (Due to the small site occupation factors and modest counting rates, relatively long measuring times were still required to observe the resonance. This could be greatly improved by increasing f through higher implantation voltages and by using higher radioactive decay rates, which should be possible, especially with shorter-lived nuclides). The decrease in signal on increasing the applied field above 0.3 T is explainable in terms of variation of the enhancement factor and thus of the saturation parameter [Eqs. (10) and (12)]. The dashed curve in Fig. 9 is fitted to the B_1(eff) dependence alone, and yields an anisotropy field of 0.42 T. The corresponding predicted signal at 1.0 T is shown in Fig. 6 for comparison; it could not be observed. If the complete expression [Eq. (12)] is used, we have two free parameters, the relaxation rate ratio a and the anisotropy field. A good fit can be obtained using reasonable combinations of values, e.g., $a = 2$, $B_a = 0.32$ T, or $a = 1.5$, $B_a = 0.38$ T; a determination of both parameters would require more data. An independent measurement of the field dependence of the relaxation rate would be useful.

The signal at 0.3 T obtained from the annealed sample was reduced to 40(15)% of the expected saturation signal. This is probably mostly due to the different rf conditions used; in particular, the rf coil was reconstructed to eliminate a power resonance and the amplitude B_1 in the sample region, which was not remeasured, may have decreased even though the input power and overall heating rate were unchanged. Also, a higher modulation frequency was used, and some dropoff due to the gaps in the rf power spectrum may have occurred. Detailed experiments with a second, slower modulaton frequency would be desirable to investigate this point.

At the ν_2 resonance ($+2 \rightarrow +1$ transition), where the relaxation time is considerably shorter, it seems likely that the signals are relaxation limited even at the higher modulation frequency. The applied B_1 amplitude may also have been lower, since it was adjusted to give tolerable nonresonant heating at the higher ν_2 frequencies in the 800-MHz region. Thus, the observed signals of about 25% saturation at 0.3 and 0.6 T are not unreasonable (Fig. 11). Here, the probable increase in relaxation time on increasing the applied field may offset the accompanying loss of enhancement factor, since the relaxtion time enters into both the modulation conditions (Fig. 5) and the saturation parameter [Eq. (12)]. The rise in signal at 0.8 T is not explained, and may be an artifact. For this subresonance, on annealing the samples, a considerable improvement in signal strength was observed (to about 66% of calculated saturation). In this case, the rf conditions for the annealed and unannealed samples were identical, so the change is due to intrinsic properties of the samples. If our hypothesis is correct and the signals are relaxation limited at this subresonance, the increase in signal is attributable to slower relaxation in the annealed sample. It is conceivable that the presence of defects in the implantation region provides a new relaxation chan-

nel which is removed on annealing, although this seems unlikely in view of the small differences in static HFI's observed. Another, more likely possibility is that the field dependence of the relaxation is affected by annealing, and the annealed sample is closer to the slower, high-field limiting relaxation rate at the applied field of 0.3 T. Again, more detailed studies of the dependence of NMR signal strength and relaxation rate on sample preparation and applied field are required to clarify this point. In any case, we have obtained satisfactory signals at both the v_1 and the v_2 subresonances with standard NMR-ON experimental conditions, and improved sample preparaton should permit a considerable reduction in counting times. Experiments with on-line implanted impurities seem quite feasible.

Nuclear moments of ^{160}Tb. The moment ratios in Table III, combined with the known nuclear moments,[57,58] of stable ^{159}Tb, permit us to calculate the nuclear moments of the ^{160}Tb 3^- ground state; we obtain $\mu(3^-) = 1.790(7)$ nm (corrected for diamagnetism) and $Q(3^-) = 3.85(5)$ b. These may be compared with those obtained from the ESR experiment of Easley *et al.*[55] Figure 12 summarizes the derived nuclear moments, using the ratios obtained from comparing the present HFI frequencies (annealed sample) with the main line (M), the low-frequency satellite (S_1), and the high-frequency satellite (S_2) from Ref. (20), as well as the HFI frequencies from precision nuclear orientation on bulk samples[33] [NO (M) compared to the main line of Ref. (20)], and the ratios of Ref. 55 [(ESR); the numbers differ slightly from those in Ref. 55 since we have recalculated them from the original data and used newer values of the ^{159}Tb reference moments].

The spread in values due to comparison with the different spectral features of the spin-echo spectra is clear from Fig. 12; it is comparable with the combined quoted errors. The bulk NO experiments are in excellent agreement with the present results, as seen also in Table III. A significant disagreement with the ESR value for the magnetic dipole moment is found. (The quadrupole moment was not determined independently in the ESR experiment of Easley *et al.*; it was found by combining the magnetic-moment ratio with an NO result, and is thus subject to the same systematic effects as the dipole moment determination.) The reason for this disagreement is not clear; the ESR experiments were difficult, involving the detection of very weak signals from radioactive Tb isotopes in the presence of a high concentration of stable ^{159}Tb, which produced broadened and dipole-split lines, but examination of the original spectra reveals no probable sources of error of the magnitude required to bring our results into agreement. The ESR results have the advantage of being obtained simultaneously for several isotopes in the same sample (we have included the values for ^{158}Tb in Fig. 12 for comparison). A similar procedure, implanting several radioactive nuclides simultaneously and measuring moment *ratios* directly, would be very desirable in future work with the present technique. We may also consider the derived nuclear moment in light of expectations from nuclear theory and systematics. The 3^- ground state of ^{160}Tb has the configuration

$\pi(\frac{3}{2} + [411]) + v(\frac{3}{2} - [521])$, $K(\pi) = 3(-)$.[57] A calculation of the magnetic moment in the Nilsson model with $\eta = +6$ was quoted in Ref. 55, giving $+2.0$ nm. Empirically, the moment of the pure $\pi(\frac{3}{2} + [411])$ state in ^{159}Tb is 2.014 nm, while those of neighboring $v(\frac{3}{2} - [521])$ states range from -0.259 to -0.44 nm, increasing with increasing neutron number (all moments corrected for diamagnetism). Neglecting odd-particle correlations, we would expect a value in the range $1.57 - 1.75$ nm; our quoted dipole moment is thus in the expected range. From the measured spectroscopic quadrupole moment, we calculate the intrinsic quadrupole moment of the 3^- state to be 9.24(12) b. The only similar states in this region whose quadrupole moments are known are the 3^+ states in ^{152,154}Eu, with two fewer protons and four and six fewer neutrons than ^{160}Tb, respectively; their intrinsic quadrupole moments are 7.58(84) and 9.36(12) b, also similar to our value. Using the rotational-model formula, we calculate the deformation parameter β for the 3^- state in ^{160}Tb to be 0.30, in excellent agreement with the systematics value for $N = 95$.[58]
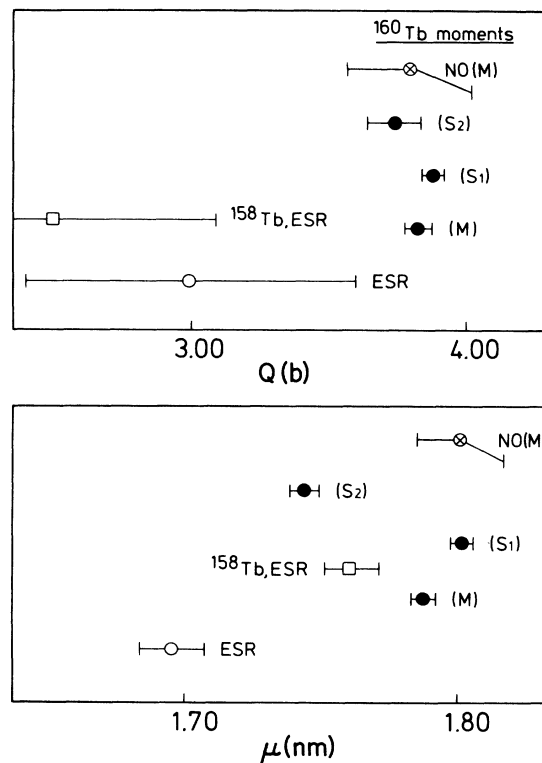

FIG. 12. Derived nuclear quadrupole moments (upper part) and magnetic moments (lower part) for the 3^- ground state of ^{160}Tb, showing the spread in values by comparing the present HFI frequencies to different features of the spin-echo spectrum of ^{159}Tb*Tb*: (M), main line; (S_1), low-frequency satellite; (S_2), high-frequency satellite. The comparison of bulk NO results with the main spin-echo lines is also shown as NO(M). ESR results for Tb doped into Nd ethylsulfate (Ref. 55) are given for ^{160}Tb, and, for comparison, for the 3^- ground state of ^{158}Tb. Numerical values for the moments were quoted in II.

CONCLUSIONS

The NMR-ON experiments described above clearly demonstrate the feasibility of applying this technique to lanthanoid impurities implanted in heavy-lanthanoid host crystals. The use of the double-resonance method at low temperatures gives reasonable signal-to-noise ratios for the simultaneous observation of two subresonances and thus permits the spectroscopic determination of both the magnetic and the quadrupole HFI frequencies in such systems. The small changes seen in the resonance frequencies and linewidths on annealing the samples, as well as the good agreement with bulk nuclear orientation results, which have very different sources of systematic errors (primarily the temperature scale), provide strong evidence that the derived HFI frequencies represent those of substitutional, undisturbed impurities and that damage to the host lattice, at least at the dose rates employed here and with room-temperature annealing, is not serious. It remains to be demonstrated whether the low-temperature implantation required for on-line NMR-ON experiments will be tolerable; experience with 3d-ferromagnetic hosts indicates that this will be the case.

The HFI frequencies obtained for ^{160}Tb*Tb* have permitted a precise evaluation of many γ-ray mixing ratios in the decay scheme of this nuclide[33] and open the possibility of its use as an absolute NO thermometer in the 10–110-mK temperature range, of particular value in high applied magnetic fields.[27] Similar experiments on other lanthanoid–heavy-lanthanoid systems will permit the development of thermometers for higher and lower temperature ranges and will facilitate nuclear-decay-scheme studies.

A factor of major importance in the NMR-ON of these systems is the sign of the quadrupole frequency v_P and the relative magnitudes of v_P and v_M. As shown by Eq. (4), a relatively large and *positive* quadrupole frequency is needed to lower the frequencies of the first subresonances, i.e., those connecting the only sublevels which are populated at the low temperatures required to produce appreciable nuclear orientaion. Otherwise, the high frequencies characteristic of the pure magnetic HFI, or even higher frequencies due to addition of the magnetic and electric HFI's, are to be expected. This would make the observation of NMR-ON rather difficult (but not necessarily impossible, since considerable rf heating can be tolerated when a large magnetic HFI is present, and the relatively shallow depth of implanted impurities under the sample surface avoids problems due to the rf skin depth, even at high resonance frequencies).

We wish to consider the extension of the double-resonance NMR-ON technique demonstrated in this work to other implanted lanthanoid (Ln) or actinoid (An) ions in HL host crystals. In Table IV we have collected data on the typical chemical, nuclear, and hyperfine interactions properties of a series of lanthanoid ions implanted in a hypothetical HL host. Tb, Dy, Ho, and Er are all suitable for this purpose, the main differences being in their magnetic properties and the ease of sample magnetization. Tb and Dy are very similar, being basal plane ferromagnets at low temperatures, which are easily

magnetized.[32,35] Gd host may also be used, as demonstrated in Ref. 11.

The second column of Table IV shows the similarities of the electronegativities and atomic volumes along the whole lanthanoid series, the exception being Eu, which is divalent in the metallic state. Implantation of any of these ions into Tb or Dy crystals, for example, should present no problems, although it is likely that Eu would enter the host lattice in the Eu^{3+} state, which has $J = 0$ and consequently no direct hyperfine interactions.

The third column gives typical nuclear spins and moment for nuclides of the given element. The first entry is usually for a stable or long-lived isotope, and the second entry for radioactive, often very short-lived nuclide. The fourth column is the magnetic HFI frequency v_M divided by the nuclear g factor and can be used to estimate v_M (in MHz) by combining with the nuclear data. The last column gives the quadrupole frequency shift (including the contribution due to the lattice ions and conduction electrons) for the first subresonance frequency, divided by $Q/4I$. Multiplying by $Q/4I$ from the nuclear-data column (Q in b) gives the frequency shift Δv_1 (MHz), and allows the first subresonance frequency v_1 to be estimated from

$$v_1 = v_M - \Delta v_1 \, ,$$

neglecting the effect of the applied field. The magnetic HFI's are all large and positive, except for the S-state ions Eu^{2+} and Gd^{3+} and the $J = 0$ ion Eu^{3+}; in the first two cases, a modest, negative magnetic hf field due to core polarization is present. The sign of the quadrupole EFG oscillates along the series.

In several cases, application of double-resonance NMR-ON will probably be difficult or impossible, because the magnetic HFI frequencies are too large and/or the quadrupole frequencies are negative. This applies to Pr, Pm, and Ho. Only if radioactive nuclides with much smaller magnetic moments are employed would the subresonance frequencies be in the range below about 1500 MHz which is readily accessible to NMR-ON. (Some favorable isotopes of Pr and Pm may exist.) Stable Nd and Sm have small quadrupole frequencies, the order of a few MHz, but these may be higher with some radioactive isotopes which have larger quadrupole moments. In any case, the magnetic HFI frequencies are below 1000 MHz, so that double-resonance NMR-ON should be feasible. The S-state ions of Eu and Gd lack the large HFI's due to the open $4f$ shells, and their electric quadrupole HFI is dominated by the lattice contribution, of order +25 MHz in HL hosts. (We have assumed that its symmetry axis is perpendicular to the quantization axis and that it can still be treated as a perturbation with respect to the magnetic interaction. This assumption will depend on the relative size of the nuclear dipole and quadrupole moments.) On the other hand, since these ions also experience only a small magnetic HFI, their magnetic frequencies are of order 100 MHz, and double-resonance experiments should be straightforward. The relaxation times may be expected to be much longer than in Tb*Tb*, which is an advantage for the observation of NMR-ON but a disadvantage for on-line implantation.

TABLE IV. Typical nuclear properties and hyperfine interactions of lanthanoid ions in HRE hosts. The nuclear spins and moments are typical values; the first line is for stable or long-lived isotopes, the second line for shorter-lived radioactive isotopes (from Ref. 57). The HFI constants are from Ref. 23; the free-ion values of the magnetic HFI were reduced by 0.92 to allow for the metallic environment. The quadrupole shifts were reduced by 0.85 in most cases, or more if necessary to give agreement with experimental values (Ref. 23), and contain estimates of the quadrupole interactions due to the crystal lattice and conduction electrons (treated as a perturbation), with symmetry axis perpendicular to the quantization axis, estimated using $(1-\gamma_\infty)=80$ and a screening factor $K=2$ (see Ref. 23).

Ion	E, V_{at} [a]	Nuclear properties I, g (nm), Q (b)	$\nu_{M/g}$ (MHz/nm)[b]	$(4I/Q)\Delta\nu_1$ [c] (MHz/b)
Pr^{3+}	1.13, 20.8	$\frac{5}{2}$, +1.6, −0.06	+2803	+1383
		2, +0.12, +0.03		
Nd^{3+}	1.14, 20.6	$\frac{7}{2}$, −0.3, −0.6	+3180	+695
		2, +0.3, −2.0		
Pm^{3+}	1.13, 22.4	$\frac{7}{2}$, +0.75, +0.7	+3170	−718
		$\frac{5}{2}$, +0.7, +1.9		
Sm^{3+}	1.17, 19.9	$\frac{7}{2}$, −0.19, +0.05	+2523	−1800
		2, +0.3, −1.3		
Eu^{2+}	1.85, 28.9	$\frac{5}{2}$, +1.0, +2.9	−267	−84
		3, +0.67, +3.9		
Eu^{3+}			0	0
Gd^{3+}	1.20, 19.9	$\frac{3}{2}$, −0.22, +2.0	−243	−84
		$\frac{5}{2}$, −0.05, +3.6		
Tb^{3+}	1.20, 19.2	$\frac{3}{2}$, +1.33, +1.43	+2340	+2840
		3, +0.6, +3.8		
Dy^{3+}	1.22, 19.0	$\frac{5}{2}$, −0.2, +2.6	+4195	+3044
Ho^{3+}	1.23, 18.7	$\frac{7}{2}$, +1.2, +3.5	+5350	+1272
Er^{3+}	1.24, 18.4	$\frac{7}{2}$, −0.16, +2.8	+5765	−1575
		4, +0.28, −2.2		
Tm^{3+}	1.25, 18.4	$\frac{3}{2}$, +0.2, −1.3	+5720	−2488
Yb^{3+}	1.25, 18.1	$\frac{5}{2}$, −0.3, +2.8	+4300	−3400
		4, +0.35, −2.3		

[a]Electronegativity of element, atomic volume (cm^3/mol).
[b]Magnetic HFI frequency/nuclear g factor.
[c]Quadrupole frequency shift of first subresonance, divided by $Q/4I$ (see text).

Tb and Dy are favorable cases, having large, positive quadrupole HFI frequencies and moderate magnetic HFI frequencies. Er and Yb are less favorable, since their quadrupole frequencies are negative, although some nuclides are known with negative quadrupole moments, which would give positive quadrupole frequencies. Furthermore, the magnetic frequencies are of order 1000 MHz, so that the subresonance frequencies may be in an acceptable range. Finally, the quadrupole interaction has not been measured for Tm (the only stable isotope has nuclear spin $\frac{1}{2}$ and thus no quadrupole moment), but interpolation indicates ν_P of about +200 MHz for a quadrupole moment of −1.0 b; this would make double-resonance NMR-ON feasible with the expected magnetic HFI frequencies of about 1200 MHz. Similar remarks apply to isotopes of Yb.

Table V contains the corresponding summary for the actinoid series; here, data are more sparse and some extrapolations have been made. The electronegativities and atomic radii of these elements are fairly similar to those in the lanthanoid series, especially for the heavier actioned ions above Am. The lighter actinoids behave chemically more like d transition elements, with small

atomic volumes and several stable valence states. Nevertheless, they should fit reasonably well and can probably be implanted sucessfully into HL crystals, although the valencies of the implanted ions are hard to predict. This probable ease of implantation is particularly true of Th, Pa, and the transplutonium elements. The more extended $5f$ shells, compared to the $4f$ shells of the lanthanoid ions, will make implanted actinoid impurities more sensitive to local environment (hybridization effects). As Table V indicates, sufficiently large quadrupole frequencies and moderate magnetic frequencies should permit double-resonance NMR-ON experiments in many such actinoid–heavy-lanthanoid systems. The small magnetic moments and large quadrupole moments typical of many actinoid nuclei are useful in this respect; particularly favorable are U, Pu, Am, Cm, and Bk. ^{252}Bk should be a good candidate, similar to (isoelectronic) Tb. An interesting case is ^{248}Cm, which, if it implants in the 3^+ state as is probable, will be an S-state ion, isoelectronic with Gd^{3+}, and should exhibit a small magnetic HFI frequency (about 60 MHz) and a quadrupole frequency ν_P near 12 MHz due to the lattice-conduction electron contribution. The resulting subresonance frequencies should

TABLE V. Properties of actinoid ions in HRE hosts. Notation as in Table IV. The HFI interactions are estimated from the free-ion data of Ref. 59, reduced as in Table IV to allow for the metallic environment. Values for Pa^{3+}, Cm^{3+} (S-state ion, isoelectronic with Gd^{3+}), and Bk^{3+} are extrapolated. The lattice-conduction electron contribution to the quadrupole HFI was estimated using $(1-\gamma_\infty)=160$, $K=2.0$.

Ion	E, V_{at}	Nuclear properties I, g(nm), Q(b)	$\nu_{M/g}$ (MHz/nm)	$(4I/Q)$ $\Delta\nu_1$ (MHz/b)
Pa^{3+}	1.3, 18.0	$\frac{7}{2}$, $+0.15$, -3.0	$(+2550)$	$(+1600)$
U^{3+}	1.38, 12.6	$\frac{7}{2}$, -0.1, $+4.5$	$+3660$	$+600$
U^{4+}			$+3440$	$+2030$
Np^{3+}	1.36, 11.6	$\frac{5}{2}$, $+1.25$, $+4.1$	$+3960$	-980
Np^{4+}			$+4410$	$+790$
Pu^{3+}	1.28, 12.3	$\frac{5}{2}$, -0.3, $+5.6$	$+3362$	-1910
Pu^{4+}			$+4630$	-1170
Am^{3+}	1.3, 17.8	$\frac{5}{2}$, $+0.64$, $+4.9$	0	0
Am^{4+}			$+3385$	-2260
Cm^{3+}	1.3, 18.0	$\frac{7}{2}$, $+0.15$, $(+5.4)$	(-324)	-168
Bk^{3+}	1.3, 18.5	$\frac{7}{2}$, $+0.56$, $+5.8$	$(+3120)$	$(+2800)$

be in the range of 100 MHz, and quadrupole relaxation may play an important role in determining τ_1. By contrast, Np and Am are not good candidates, unless nuclear states with very small magnetic moments can be found.

Finally, we emphasize again the importance of careful cleaning of the sample crystals before implantation and of the use of high-implantation voltages to give large-site-occupation factors. With these precautions, on-line applications of the technique should be successful. Furthermore, in cases with fast nuclear relaxation, which will generally be present for non-S-state lanthanoid and actinoid ions in HL hosts, a high modulation frequency ν_{fm} (5 kHz or more) should be used, with a second, lower modulation frequency superposed to close the gaps in the rf power spectrum.

ACKNOWLEDGMENTS

[1]E. Mathias and R. J. Holliday, Phys. Rev. Lett. **17**, 897 (1966).

[2]J. E. Templeton and D. A. Shirley, Phys. Rev. Lett. **18**, 240 (1967).

[3]N. J. Stone, in *Low Temperature Nuclear Orientation*, edited by N. J. Stone and H. Postma (North-Holland, Amsterdam, 1986), Chap. 13, p. 641; D. H. Chaplin and G. V. H. Wilson, in *ibid.*, Chap. 14, p. 693.

[4]P. Herzog, in Ref. 3, Chap. 15, p. 731; N. J. Stone, in *Site Characterization and Aggregation of Implanted Atoms in Materials*, edited by A. Perez and R. Coussement (Plenum, New York, 1980), p. 189.

[5]P. Herzog, in Ref. 3, Appendix 3, p. 953.

[6]J. Dupak, M. Finger, V. N. Pavlov, M. Rotter, and B. Sedlak, Acta Phys. Slovaka **31**, 167 (1981); J. Rikovska, A. Machova, D. Novakouva, J. Ferencei, and M. Finger, Hyperfine Interactions **15/16**, 83 (1983).

[7]T. I. Kracikova, S. Davaa, M. Finger, and V. A. Deryaga, Hyperfine Interactions **15/16**, 73 (1983).

[8]I. Berkes, R. Brenier, and G. Marest, J. Phys. G **9**, 213 (1983).

[9]W. van Rijswijk, F. G. van den Berg, W. R. Joosten, and W. J. Huiskamp, Hyperfine Interactions **15/16**, 325 (1983).

[10]P. Herzog, U. Daemmrich, K. Freitag, C.-D. Herrmann, and K. Schloesser, Hyperfine Interactions **22**, 167 (1985).

[11]K.-H. Ebeling, R. Eder, E. Hagn, E. Zech, and M. Deicher, Phys. Rev. Lett. **54**, 2135 (1985).

[12]P. T. Callaghan, W. M. Lattimer, P. D. Johnston, and N. J. Stone, Hyperfine Interactions **2**, 288 (1976).

[13]E. Hagn and E. Zech, Z. Phys. A **307**, 159 (1982); Phys. Rev. B **29**, 1148 (1984); E. Hagn, K. Leuthold, E. Zech, and H. Ernst, Z. Phys. A **295**, 385 (1980); E. Hagn and E. Zech, *ibid.* **297**, 329 (1980); R. Eder, E. Hagn, and E. Zech, Phys. Rev. C **32**, 582 (1985).

[14]S. Ohya, S. Ohtake, K. Nishimura, and N. Mutsuro, Phys. Rev. C **36**, 2072 (1987); S. Ohya, S. Suzuki, K, Nishimura, and N. Mutsuro, J. Phys. G (to be published).

[15]R. Eder, E. Hagn, and E. Zech, Phys. Lett. **158B**, 371 (1985); K. Nishimura, S. Ohya, and N. Mutsuro, Hyperfine Interactions **36**, 235 (1987).

[16]S. Ohya, K. Nishimura, and N. Nutsuro, Hyperfine Interactions **39**, 193 (1988).

[17]K. H. Ebeling, R. Eder, E. Hagn, E. Zech, and M. Deicher, Z. Naturforsch. **41a**, 95 (1986).

[18]W. D. Brewer and E. Wehmeier, Phys. Rev. B **12**, 4608 (1975).

[19]M. Weger, Phys. Rev. **128**, 1505 (1962).

[20]N. Sano and J. Itoh, J. Phys. Soc. Jpn. **32**, 95 (1972).

[21]B. Bleaney, in *Proceedings of the Third Quantum Electronics*

Conference, Paris, 1963, edited by P. Grivet and N. Bloembergen (Columbia University Press, New York, 1964).

[22]S. A. Ahmad, W. Klempt, C. Ekström, R. Neugart, and K. Wendt, Z. Phys. A **321**, 35 (1985); see also P. Aufmuth, K. Heilig, and A. Steudel, At. Data Nucl. Data Tables **37**, 455 (1987).

[23]B. Bleaney, in *Magnetic Properties of Rare Earth Metals,* edited by R. J. Elliott (Plenum, London, 1972), p. 383.

[24]S. Kobayashi, N. Sano, and J. Itoh, J. Phys. Soc. Jpn. **23**, 474 (1967).

[25]N. Sano, S. Kobayashi, and J. Itoh, Prog. Theor. Phys. Suppl. **46**, 84 (1970).

[26]I. S. Mackenzie, M. A. H. McCausland, and A. R. Wagg, J. Phys. F **4**, 315 (1974).

[27]H. Marshak, in Ref. 3, Chap. 16, p. 769; H. Marshak, W. D. Brewer, P. Roman, and M. Böttcher, Jpn. J. Appl. Phys. **26**, CQ14 (1987).

[28]K. S. Krane, Nucl. Phys. **A377**, 176 (1982).

[29]H. Marshak, Hyperfine Interactions **15/16**, 1043 (1983).

[30]P. Roman, W. D. Brewer, E. Klein, H. Marshak, K. Freitag, and P. Herzog, Phys. Rev. Lett. **56**, 1976 (1986).

[31]H. Marshak, W. D. Brewer, P. Roman, E. Klein, K. Freitag, and P. Herzog, Phys. Rev. Lett. **59**, 1764 (1987).

[32]J. Grimm, J. Boysen, W. D. Brewer, and G. V. H. Wilson, J. Phys. F **13**, 1931 (1983).

[33]H. Marshak, W. D. Brewer, and P. Roman (unpublished).

[34]Button No. BB-22-34, grown by the recrystallization method; purity: < 18 ppm other RE, < 33 ppm 0, < 8 ppm C, < 8.5 ppm Fe.

[35]H. Marshak, P. Roman, and W. D. Brewer, Hyperfine Interaction (to be published).

[36]K. Freitag, Radiat. Eff. **44**, 185 (1979).

[37]G. Sidenius and O. Skilbreid, in *Electromagnetic Separation of Radioactive Isotopes,* edited by M. J. Higatsberger and F. P. Viehböck (Springer, Vienna, 1961), p. 243.

[38]A. Abragam, *The Principles of Nuclear Magnetism* (Oxford University Press, Oxford, 1961).

[39]R. G. Barnes, in *Handbook on tthe Physics and Chemistry of Rare Earths,* edited by K. A. Gschneidner, Jr. and L. Eyring (North-Holland, Amsterdam, 1979), p. 387.

[40]P. D. Johnston, R. A. Fox, and N. J. Stone, J. Phys. C. **5**, 2077 (1972).

[41]N. J. Stone, Hyperfine Interactions **8**, 83 (1980).

[42]E. Hagn, Phys. Rev. B **25**, 1521 (1982); E. Hagn and E. Zech, *ibid.* **25**, 1529 (1982).

[43]E. Hagn, Hyperfine Interactions **22**, 19 (1985).

[44]Y. Seiwa, T. Tsuda, A. Hirai, and C. W. Searle, Phys. Lett. **43A**, 23 (1973).

[45]J. Durand and C. Robert, J. Phys. F **3**, L90 (1973).

[46]M. A. H. McCausland and I. S. Mackenzie, Adv. Phys. **28**, 305 (1979).

[47]R. J. Blin-Stoyle and M. A. Grace, in *Handbuch der Physik,* *XLII,* edited by S. Flügge (Springer-Verlag, Berlin, 1955), p. 555.

[48]F. Bacon, J. A. Barclay, W. D. Brewer, D. A. Shirley, and J. E. Templeton, Phys. Rev. B **5**, 2397 (1972).

[49]E. Klein, in Ref. 3, Chap. 12, p. 579; Hyperfine Interactions **15/16**, 557 (1983).

[50]G. V. H. Wilson, J. A. Barclay, and C. G. Don, Phys. Rev. B **6**, 729 (1972).

[51]E. Klein (private communication); J. A. Barclay, Ph.D. thesis, University of California at Berkeley, 1969.

[52]W. D. Brewer, D. A. Shirley, and J. E. Templeton, Phys. Lett. **27A**, 81 (1968).

[53]M. Sablik, S. Skalski, and J. I. Budnick, Phys. Rev. B **8**, 2222 (1973).

[54]G. V. H. Wilson and J. Bosse, Phys. Rev. B **10**, 1854 (1974).

[55]W. C. Easley, J. A. Barclay, and D. A. Shirley, Phys. Rev. **170**, 1083 (1968).

[56]M. Kopp and W. D. Brewer, Hyperfine Interactions **3**, 321 (1977).

[57]*Table of Isotopes,* edited by C. M. Lederer and V. S. Shirley (Wiley, New York, 1978).

[58]Y. Tanaka, R. M. Steffen, E. B. Shera, W. Reuter, M. V. Hoehn, and J. D. Zumbro, Phys. Rev. Lett. **51**, 1633 (1983); Phys. Rev. C **29**, 1830 (1983).

[59]B. D. Dunlap and G. M. Kalvius, in *The Actinides: Electronic Structure and Related Properties,* edited by A. J. Freeman and J. B. Darby, Jr. (Academic, New York, 1974), p. 237.